NACA RM L55H02

NACA

RESEARCH MEMORANDUM

FREE-FLIGHT TESTS TO DETERMINE THE POWER-ON AND POWER-OFF PRESSURE DISTRIBUTION AND DRAG OF THE NACA RM-10 RESEARCH VEHICLE AT LARGE REYNOLDS NUMBERS BETWEEN MACH NUMBERS 0.8 AND 3.0

By Sherwood Hoffman

Langley Aeronautical Laboratory
Langley Field, Va.

NATIONAL ADVISORY COMMITTEE
FOR AERONAUTICS

WASHINGTON

September 20, 1955
Declassified August 16, 1957

NATIONAL ADVISORY COMMITTEE FOR AERONAUTICS

RESEARCH MEMORANDUM

FREE-FLIGHT TESTS TO DETERMINE THE POWER-ON AND POWER-OFF PRESSURE DISTRIBUTION AND DRAG OF THE NACA RM-10 RESEARCH VEHICLE AT LARGE REYNOLDS NUMBERS BETWEEN MACH NUMBERS 0.8 AND 3.0

By Sherwood Hoffman

SUMMARY

The effect of a propulsive jet on the drag and pressure distribution of the NACA RM-10 missile configuration at large Reynolds numbers has been determined by flight tests of rocket models between Mach numbers 0.8 and 3.0. Pressures were measured along the body, near the fin root, and at the base. The jet pressure ratio and jet exit Mach number were of the order of 1.5 and 3.5. The Reynolds number varied from about 60×10^6 to 220×10^6, based on body length.

Jet interference resulted in large increases in base pressure between Mach numbers 0.8 and 3.0 with base thrust being obtained below Mach number 1.8. The jet effects produced large increases in pressure at the rearmost stations on the afterbody and fin root at the transonic and low-supersonic portions of the Mach number range. The total drag of the configuration between Mach numbers 1.8 and 3.0 was reduced by about 15 percent, which was due to favorable jet interference at the base. The measured body and fin pressures are compared with those obtained from linearized theory and from various wind-tunnel tests at supersonic speeds.

INTRODUCTION

Recent investigations (refs. 1 to 5) of bodies with flow issuing from the base have shown that a jet may produce large changes in the drag and pressure distribution of a configuration at transonic and supersonic speeds. Because there are many factors involved in the jet interference problem, such as nozzle design, jet operating conditions, and afterbody shape, a great deal of work is being done to provide a

better understanding of the jet interference phenomena and to obtain useful data for the design of aircraft having a minimum of unfavorable jet effects.

In recognition of the need for more interference studies for both the power-on and power-off flight conditions, the Pilotless Aircraft Research Division has undertaken several investigations of jet effects at high Mach numbers and Reynolds numbers. The present paper reports on the flight tests of two rocket-propelled full-scale NACA RM-10 models that were instrumented to measure body pressure distribution, fin root pressures, base pressure, and drag for both power-on and power-off flight. The NACA RM-10 research vehicle was selected for this jet effect investigation because a great deal of basic research has been done with it under power-off conditions (refs. 6 to 23), especially with regard to its drag at supersonic speeds. The present tests covered continuous ranges of Mach number between 0.8 and 3.0 with corresponding Reynolds numbers varying from about 60×10^6 to 220×10^6 based on body length. The jet static pressure ratio and jet exit Mach number of the test vehicles were approximately 1.5 and 3.5, respectively. The measured pressure distributions are compared with those obtained for power off from various wind-tunnel tests at lower Reynolds numbers and with linearized theory at supersonic speeds. The effect of the jet on the body, fin, and base drags is determined through a breakdown of the drag components as determined from the pressure measurements and linearized theory for the body and fins through most of the Mach number range.

The models were flight tested at the Langley Pilotless Aircraft Research Station at Wallops Island, Va.

SYMBOLS

A	maximum cross-sectional area of body, 0.785 ft^2
b	span of fins, 35.88 in.
c	streamwise chord of fins, 18.14 in.
C_D	total drag coefficient, based on A
C_{D_p}	body pressure drag coefficient, based on A
C_{D_B}	base drag coefficient, based on A
C_{D_f}	friction drag coefficient of body, based on A

C_f average skin-friction coefficient based on wetted area of body

C_p pressure coefficient, $\frac{p - p_l}{q_l}$

ΔC_p jet-effect pressure coefficient, $C_{p_{\text{jet on}}} - C_{p_{\text{jet off}}}$

L length of body, 146.5 in.

M Mach number

p local static pressure, lb/ft^2

p_l free-stream static pressure, lb/ft^2

p_j jet static pressure, lb/ft^2

q_l free-stream dynamic pressure, lb/ft^2

R Reynolds number, based on L in feet

r local radius of body, in.

T time, sec

T_l free-stream temperature, ^oF abs

T_W average temperature of skin of body, ^oF abs

T_{AW} adiabatic wall temperature, ^oF abs

x station measured from body nose, in.

X station measured from fin leading edge, in.

y fin plan-form ordinate, measured from body center line, in.

ϕ body polar angle (deg) measured from fin plane in counterclockwise direction ($\phi = 0^o$ at top fin in vertical plane)

MODELS

Details, dimensions, and photographs of the two NACA RM-10 models tested are given in figures 1 to 3. The bodies were derived from a parabolic arc of revolution of fineness ratio 15 by cutting off part of the pointed stern to allow space for the rocket jet. The resulting model had a fineness ratio of 12.2 and maximum body diameter of 12 inches. The configuration was stabilized by four 60° sweptback, untapered fins of aspect ratio 2.04. The airfoil of the fins consisted of a 10-percent-thick circular-arc cross section normal to the leading edge or 5 percent thick in the streamwise direction. Both models were constructed of spun magnesium alloy skins and cast magnesium tail cones to which the cast magnesium fins were attached.

Model A was instrumented to measure 18 body pressures, base pressure, nozzle pressure, free-stream static pressure, eight fin pressures, acceleration during thrusting flight, and deceleration (drag acceleration) during coasting flight. Thirteen of the body orifices were located in a plane 45° (ϕ = 45°) between the fins (fig. 1(a)). At stations x/L = 0.921 and 0.986 (fig. 1(b)), orifices were installed at ϕ = 15°, 30°, and 45°. The side pressure orifice at x/L = 0.998 was at ϕ = 30°. All the body orifice stations are tabulated in table I.

The fin pressure measurements (fig. 1(b)) were taken at four chordwise stations and two spanwise stations. The latter stations were located at 1 inch and 3 inches from the body (at the fin root) measured parallel to the leading edge. The orifice stations on the fins are tabulated in table II.

Model B was equipped to measure 10 pressures on the afterbody and base pressure (fig. 2(a)). These stations were selected to supplement the measurements taken on model A and provide check points at x/L = 0.884 (ϕ = 45°), 0.952 (ϕ = 45°), and 0.986 (ϕ = 15°). The orifice stations on model B are tabulated in table III.

The base pressures on both models were taken by single orifice measurements as is shown in figures 1(c) and 2(b). Although the base pressure orifices are in different locations inside the stern of each model, the results of the present tests indicate that each position was equally efficient in measuring the pressures.

Both models were equipped with 6-inch ABL Deacon rocket motors, but with slightly different grain construction of the propellant. The propellant used for model A was cast while that for model B was extruded. This difference in grain construction necessitated the use of slightly different nozzle designs (figs. 1(c) and 2(b)) for optimum performance of the motors.

Four equally spaced jet orifices, manifolded to a pressure cell, were used to measure the wall pressures near the exit of the nozzle of model A as is shown in figure 1(c).

TESTS AND MEASUREMENTS

The models were tested at the Langley Pilotless Aircraft Research Station at Wallops Island, Va. Model A was propelled by a two-stage rocket system (fig. 3(c)) that consisted of a 6-inch ABL Deacon rocket motor booster and sustainer rocket motor. Model B was propelled by one stage, the rocket motor in its fuselage. Velocity and trajectory data were obtained from the CW Doppler velocimeter and the NACA modified SCR 584 tracking radar unit, respectively. A survey of atmospheric conditions including winds aloft was made by radiosonde measurements from an ascending balloon that was released before each test.

Both models were equipped with multichannel telemetering systems to transmit the measured pressures and accelerations to a ground receiving station. Model A, which was the principal test vehicle of this investigation, had 31 channels of telemetering compared to 11 for model B. At the start of the test of model A, two pressure channels shorted out; and, as a consequence, no data were received for the body orifices at $x/L = 0.068$ ($\phi = 45^\circ$) and 0.986 ($\phi = 45^\circ$). The time-lag constant for the pressure system of both models was less than 0.007 second, which was sufficiently small to allow pickup of the rapid changes in pressure obtained during accelerating flight.

The body and fin pressure coefficients of model A were based on the static tube measurements of free-stream static pressure. These coefficients were compared with those obtained using the radiosonde measurements of p_1 at several orifice stations and were found to agree within the accuracy of the tests through most of the speed range. The agreement thus obtained is indicative of the accuracy of the pressure coefficients for model B which did not have a static pressure tube.

The jet-off drag coefficients of the models were determined during decelerating flight by the method described in reference 24. For comparative purposes, the jet-off drags were evaluated using the decelerations as determined by the drag accelerometers and by differentiating the velocity time curve of CW Doppler radar. Since the latter instrument failed to track either model beyond approximately 13 seconds, the differentiated velocity curve was useful for checking the telemetered decelerations only from Mach number 3.0 to 2.0. Below this range, the magnitude of the deceleration of both models was small and only slightly greater than the accuracy of the drag accelerometer. The resulting jet-off drag coefficients were questionable and, hence, are not included

herein. The jet-on acceleration and nozzle static pressure were measured on model A in an attempt to evaluate the power-on drag of the configuration.

The Mach number ranges, Reynolds number ranges, and free-stream conditions for the tests are presented in figure 4. The jet-on test range for model A varied between Mach numbers 1.1 and 3.0 and Reynolds numbers 70×10^6 and 220×10^6; and for model B between Mach numbers 0.8 and 2.6 with corresponding Reynolds numbers from 60×10^6 to 210×10^6. For the decelerating part of the tests, the aforementioned ranges were essentially reversed in flight.

The following table gives an estimation of the accuracy of the coefficients, based on instrument accuracy, for the flight tests:

C_p	±0.01
C_D (supersonic) $(2.0 \leq M \leq 3.0)$	±0.005
C_{D_B} (supersonic)	±0.003
C_{D_B} (transonic)	±0.005

The Mach number is estimated to be accurate within ±0.01 through a considerable part of the Mach number range.

RESULTS AND DISCUSSION

Basic Data

The variations of the measured pressure coefficients with Mach number for each orifice station on models A and B are presented in figures 5, 6, and 7. The pressure coefficients obtained for both jet-on and jet-off conditions are compared in each plot. An examination of these results shows that large differences in the afterbody pressures and fin pressures were obtained between the jet-on and jet-off conditions at low supersonic and transonic speeds, with the greatest differences being measured at the rearmost body orifices and fin orifices and at the base. The following sections are devoted to a more detailed study of these pressures in order to determine the effect of the jet on the power-off pressure drag and total drag of the NACA RM-10 body.

Body Pressures

The pressure coefficients measured on the body of model A at $\phi = 45^\circ$ are compared with the theoretical body pressures as determined by linearized theory (ref. 25) and the method of characteristics (ref. 26) at Mach numbers 1.2, 1.5, 2.0, 2.5, and 3.0 in figure 8. The pressures at $\phi = 15^\circ$ and 30° have been omitted from this figure to avoid a congestion of test points in the afterbody region. The deviation between the theory and experiment at stations forward of the fins is consistent with that obtained in wind-tunnel investigations (refs. 8 and 10) of the RM-10 body without fins. These comparisons and figure 5 also show that the jet-on and jet-off pressure distributions are the same, except on the afterbody at low supersonic and transonic Mach numbers.

The effect of the jet on the afterbody and base pressures of models A and B may be seen more clearly by comparing the variations of ΔC_p (jet effect coefficient) with Mach number in figures 9 and 10. The positive values of ΔC_p represent an increase in pressure due to the jet issuing from the base. As is shown in references 1 and 4, the interaction effect of the jet on the afterbody is largely a function of body geometry and jet pressure ratio. The present results are in general agreement with tests of similar configurations having a low boattail angle and small annulus base in that the jet affected primarily the base and side pressures at supersonic speeds. Also, the jet affected the afterbody at all radial stations with nearly the same intensity as may be seen by comparing the variations of ΔC_p for $x/L = 0.952$ at $\phi = 15^\circ$, 30°, and 45° in figure 10. The largest jet interference occurred between Mach numbers 0.8 and 1.2 for each station and then the interference decreased with increasing Mach number.

Figure 11 shows comparisons of the jet to free-stream static pressure ratios and the variations of ΔC_p for corresponding body orifices on models A and B. The jet exit pressures used for obtaining p_j/p_1 and the jet pressure coefficient (fig. 9(d)) for model A were computed for the exit of the nozzle using the measured nozzle pressures and a ratio of specific heats of 1.28. The jet pressure ratios for model B were estimated from the known characteristics of the rocket motor and the trajectory of the model. The comparison in figure 11(a) shows that the jet pressure ratios thus obtained agreed within 20 percent between Mach numbers 1.2 and 2.5. Owing to the small magnitude of p_j/p_1, the differences obtained would have a negligible effect on the jet effects of the models at corresponding Mach numbers. However, there was a significant difference in the jet exit Mach numbers due to changing the propellant. Model A had the cast grain propellant which gave a ratio of chamber pressure to exit static of 61 in contrast to a ratio of 51 for the extruded grain of model B. The corresponding jet exit Mach numbers were about 3.6 and 3.1, respectively.

According to reference 3, changing the jet exit Mach number at a nearly constant jet to free-stream static pressure ratio and free-stream Mach number would change the jet boundary and hence the interference from the jet. This may account for the different levels of ΔC_p obtained at the base and corresponding afterbody stations of the models as is shown in figures 11(b) to 11(e). The change in jet exit Mach number evidently had little or no effect on the afterbody pressures above $M = 1.4$, whereas a marked effect is shown at the base up to the limits of the tests.

Fin Pressures

The variations of the fin pressure coefficients with Mach number for model A are shown in figure 6. Cross plots of these variations at Mach numbers 1.2, 1.5, 2.0, 2.5, and 3.0 are presented in figure 12 for the orifices 1 inch from the body (measured parallel to leading edge) and in figure 13 for the orifices 3 inches from the body. These experimental points are compared with the theoretical chordwise pressure distributions for isolated fins as determined by linearized wing theory (refs. 27 and 28), except at Mach number 2.0 where the theoretical values become infinite. At this Mach number, the Mach lines were alined with the 60° swept-back, untapered fins. For the present application, it was assumed that the body acted as a reflection plane or that the exposed, opposite fins had a common root chord at the body surface. Since the orifices were not parallel to the free-stream direction, an average semispan location was used for each reference chord in order to simplify the computations. The average semispan distances are referred to the center line of the body, for convenience, in the figures and are $\left(\frac{y}{b/2}\right)_{average} = 0.27$ and 0.33 for the two chords.

The agreement obtained between the theory and tests (figs. 12 and 13) for either the jet-on or jet-off condition at Mach numbers 1.2 and 1.5 is reasonably good in view of the interference effects from the afterbody and jet. It should be noted, also, that the fin orifices at $\left(\frac{y}{b/2}\right)_{average} = 0.27$ were in the relatively thick turbulent boundary layer of the afterbody. According to measurements made in reference 22, the boundary-layer thickness would vary from about 1.0 inch at $M = 1.0$ to 1.5 inches at $M = 3.0$. At Mach numbers 2.5 and 3.0, where no jet interference was measured, the fin pressures are lower than those calculated by an amount approximately equal to the pressures on the isolated body (ref. 8 or 10, or fig. 8) at corresponding stations.

A comparison of the jet effect pressure coefficients in figure 14 shows the same general variations of ΔC_p with Mach number as was obtained

on the afterbody; namely, the jet interference was large at the lower supersonic speeds and at transonic speeds. The effect of small trim changes during thrusting flight on ΔC_p, especially at transonic speeds, was estimated to have small effect on the jet pressure coefficients of the fins and to be less than the accuracy of the measurements.

Drag

The variations of total drag coefficient and base drag coefficient with Mach number for the jet-off condition are shown in figure 15. A comparison of the present results shows that excellent agreement was obtained between models A and B above $M \cong 2.0$ for total drag and throughout the supersonic speed range for base drag. The data below $M \cong 2.0$ for total drag were omitted because of questionable accelerometer measurements. Also given in this figure is a comparison of the present data with the total drag and base drag coefficients of four similar flight models from references 6 and 11. The referenced curves are in good agreement with the test results through corresponding ranges of Mach number, thus making it possible to extend the total drag curve of models A and B to Mach number 0.9.

Two methods were employed for obtaining the power-on drag coefficient of the RM-10 configuration. The first one, discussed in reference 29, requires the computation of the thrust to a high degree of accuracy in order to determine the drag. Although the characteristics of the rocket motor used were known, it was not possible to compute thrusts that would give accurate values of drag. As a consequence, these drags are not presented herein. For the second approach to the problem, it was necessary to reconstruct the total drag for power-on by computing the pressure, friction, and base drags, and by estimating the fin-plus-interference drag from a breakdown of C_D for the power-off flight condition.

The body pressure drag for the configuration was computed from curves faired through the experimental values of C_p of model A at several supersonic Mach numbers and is presented in figure 16. The solid curve in this figure shows that the jet did not affect the pressure drag above Mach number 2.0. The curve is dotted below Mach number 2.0 to indicate that the jet had a small but negligible effect on reducing the power-off pressure drag. The reduction in C_{D_p} due to the jet was approximately equal to the accuracy of the tests. Figure 16 also shows that the pressure drag was about 10 percent higher than that obtained from four different wind-tunnel tests (refs. 9, 10, 14, and 16) and from theory for configuration without fins. This difference may be due to interference obtained from the nose static tube of the flight model.

The variations of base drag coefficient with Mach number for both models are given in figure 17. The annulus area of each model was used in computing the base drag during thrusting flight, while the entire base area was used for the jet-off portion of the tests. The comparisons in figure 17 show that the jet eliminated the base drag on both models throughout the Mach number range and produced base thrust below Mach number 1.8.

The friction drag coefficient was computed for model A by using the empirical method of reference 17. This method involves a step-by-step computation with time of C_f, based on the calculated values of average skin temperature and the measured values of Mach number and Reynolds number along the trajectory. The heat-transfer coefficients used for determining the average skin temperatures and wall heating parameter (shown in fig. 18(a)) were Van Dreist's theoretical flat-plate turbulent heat-transfer coefficients assuming turbulent flow from the nose. The adiabatic wall temperatures shown were determined assuming a temperature recovery factor of 0.9. The average Reynolds numbers were taken at station $x/L = 0.525$ which is the average area station of the body. The variations of C_f with M thus obtained for the jet-on and jet-off conditions, given in figure 18(b), show little change in skin friction under the different wall heating conditions. Also shown in this last figure is the measured variation of C_f of a similar model with jet off tested in reference 17 (model 5) under slightly different flight conditions. Since small changes in flight conditions would not appreciably affect the skin friction, this curve is presented to show that the computed values of C_f are in agreement with those measured in the referenced paper.

The power-off drag of the fins plus interference was obtained by subtracting the base, pressure, and friction drag coefficients from the average total drag coefficient (fig. 15) through a range of Mach number from 1.15 to 3.0 as is shown in figure 19(a). In order to estimate the effect of the jet on the power-off fin drag and hence the total drag, a study was made of possible shock patterns near the base of the configuration. Figure 20 shows the estimated location of the shock wave based on the variations of the afterbody and fin pressures at Mach numbers near 1.0, 1.2, 2.0, and 3.0. It appears that the shock wave near Mach numbers 1.0 and 1.2 sweeps spanwise across the fins causing considerable interference for both jet-on and jet-off conditions. For these Mach numbers, the results indicate that the jet caused the shock wave to move upstream slightly and, thus, change the interference effects. The magnitude of the interference at these Mach numbers could not be estimated from the limited data obtained, but it appears that the effect would be favorable from a drag standpoint. At the higher Mach numbers, where the measured pressures were not affected by the jet, except at the base, the shock wave was either inclined along the fin trailing edge or farther

downstream as is shown in figure 20. For this condition, the change in fin drag caused by the jet would probably be negligible.

The foregoing discussion permits an estimation of the jet on total C_D (fig. 19(b)) by summing the drag components at supersonic speeds. For a range of Mach number from about 1.8 to 3.0, the jet reduced the total drag by about 15 percent, which was due to favorable interference at the base. Between Mach numbers 1.15 and 1.8, the pressure measurements indicate a greater reduction in total drag due to favorable interference at the base, afterbody, and fins (not shown in fig. 19(b)). At Mach numbers below 1.15, the supplemental data taken from model B indicate that jet interference would give a marked reduction in total C_D especially near Mach number 1.0.

CONCLUSIONS

The effect of a propulsive jet on the pressure distribution and drag of the NACA RM-10 missile configuration has been investigated by flight tests of instrumented rocket-propelled models through a range of Mach number from 0.8 to 3.0 and Reynolds number from about 60×10^6 to 220×10^6 based on body length. The jet pressure ratio and jet exit Mach number were of the order of 1.5 and 3.5, respectively. The following results are indicated:

1. Jet interference resulted in large increases in base pressure between Mach numbers 0.8 and 3.0 with base thrust being obtained below Mach number 1.8.

2. The jet effects produced large increases in pressure at the rearmost stations on the afterbody and fin root at the transonic and low-supersonic portions of the Mach number range.

3. The total drag of the configuration between Mach numbers 1.8 and 3.0 was reduced by about 15 percent, which was due to favorable jet interference at the base.

Langley Aeronautical Laboratory,
National Advisory Committee for Aeronautics,
Langley Field, Va., July 19, 1955.

REFERENCES

1. Gillespie, Warren, Jr.: Jet Effects on Pressures and Drags of Bodies. NACA RM L51J29, 1951.

2. De Moraes, Carlos A., and Nowitzky, Albin M.: Experimental Effects of Propulsive Jets and Afterbody Configurations on the Zero-Lift Drag of Bodies of Revolution at a Mach Number of 1.59. NACA RM L54C16, 1954.

3. Love, Eugene S., and Grigsby, Carl E.: Some Studies of Axisymmetric Free Jets Exhausting From Sonic and Supersonic Nozzles Into Still Air and Into Supersonic Streams. NACA RM L54L31, 1955.

4. Cortright, Edgar M., Jr., and Schroeder, Albert H.: Investigation at Mach Number 1.91 of Side and Base Pressure Distributions Over Conical Boattails Without and With Jet Flow Issuing From Base. NACA RM E51F26, 1951.

5. Henry, Beverly Z., Jr., and Cahn, Maurice S.: Preliminary Results of an Investigation at Transonic Speeds to Determine the Effects of a Heated Propulsive Jet on the Drag Characteristics of a Related Series of Afterbodies. NACA RM L55A24a, 1955.

6. Evans, Albert J.: The Zero-Lift Drag of a Slender Body of Revolution (NACA RM-10 Research Model) as Determined From Tests in Several Wind Tunnels and in Flight at Supersonic Speeds. NACA Rep. 1160, 1954. (Supersedes NACA TN 2944.)

7. Carros, Robert J., and James, Carlton S.: Some New Drag Data on the NACA RM-10 Missile and a Correlation of the Existing Drag Measurements at $M = 1.6$ and 3.0. NACA TN 3171, 1954.

8. Cooper, Morton, Gapcynski, John P., and Hasel, Lowell E.: A Pressure Distribution Investigation of a Fineness-Ratio-12.2 Parabolic Body of Revolution (NACA RM-10) at $M = 1.59$ and Angles of Attack up to 36°. NACA RM L52G14a, 1952.

9. Hasel, Lowell E., Sinclair, Archibald R., and Hamilton, Clyde V.: Preliminary Investigation of the Drag Characteristics of the NACA RM-10 Missile at Mach Numbers of 1.40 and 1.59 in the Langley 4- by 4-Foot Supersonic Tunnel. NACA RM L52A14, 1952.

10. Love, Eugene S., Coletti, Donald E., and Bromm, August F., Jr.: Investigation of the Variation With Reynolds Number of the Base, Wave, and Skin-Friction Drag of a Parabolic Body of Revolution (NACA RM-10) at Mach Numbers of 1.62, 1.93, and 2.41 in the Langley 9-Inch Supersonic Tunnel. NACA RM L52H21, 1952.

11. Jackson, H. Herbert, Rumsey, Charles B., and Chauvin, Leo T.: Flight Measurements of Drag and Base Pressure of a Fin-Stabilized Parabolic Body of Revolution (NACA RM-10) at Different Reynolds Numbers and at Mach Numbers From 0.9 to 3.3 NACA TN 3320, 1954. (Supersedes NACA RM L50G24.)

12. Piland, Robert O.: Drag Measurements on a 1.16-Scale, Finless, Sting-Mounted NACA RM-10 Missile in Flight at Mach Numbers From 1.1 to 4.04 Showing Some Reynolds Number and Heating Effects. NACA RM L54H09, 1954.

13. Luidens, Roger W., and Simon, Paul C.: Aerodynamic Characteristics of NACA RM-10 Missile in 8- by 6-Foot Supersonic Wind Tunnel at Mach Numbers From 1.49 to 1.98. I - Presentation and Analysis of Pressure Measurements (Stabilizing Fins Removed). NACA RM E50D10, 1950.

14. Esenwein, Fred T., Obery, Leonard J., and Schueller, Carl F.: Aerodynamic Characteristics of NACA RM-10 Missile in 8- by 6-Foot Supersonic Wind Tunnel at Mach Numbers From 1.49 to 1.98. II - Presentation and Analysis of Force Measurements. NACA RM E50D28, 1950.

15. Coletti, Donald E.: Investigation of the Aerodynamic Characteristics of the NACA RM-10 Missile (With Fins) at a Mach Number of 1.62 in the Langley 9-Inch Supersonic Tunnel. NACA RM L52J23a, 1952.

16. Perkins, Edward W., Gowen, Forrest E., and Jorgensen, Leland H.: Aerodynamic Characteristics of the NACA RM-10 Research Missile in the Ames 1- by 3-Foot Supersonic Wind Tunnel No. 2 - Pressure and Force Measurements at Mach Numbers of 1.52 and 1.98. NACA RM A51G13, 1951.

17. Loposer, Dan J., and Rumsey, Charles B.: Flight Measurements of Average Skin-Friction Coefficients on a Parabolic Body of Revolution (NACA RM-10) at Mach Numbers From 1.0 to 3.7. NACA RM L54G14, 1954.

18. Rumsey, Charles B., and Loposer, J. Dan: Average Skin-Friction Coefficients From Boundary-Layer Measurements in Flight on a Parabolic Body of Revolution (NACA RM-10) at Supersonic Speeds and at Large Reynolds Numbers. NACA RM L51B12, 1951.

19. Maloney, Joseph P.: Drag and Heat Transfer on a Parabolic Body of Revolution (NACA RM-10) in Free Flight to Mach Number 2 With Both Constant and Varying Reynolds Number and Heating Effects on Turbulent Skin Friction. NACA RM L54D06, 1954.

20. Chauvin, Leo T., and DeMoraes, Carlos A.: Correlation of Supersonic Convective Heat-Transfer Coefficients From Measurements of the Skin Temperature of a Parabolic Body of Revolution (NACA RM-10). NACA RM L51A18, 1951.

21. Czarnecki, K. R., and Marte, Jack E.: Skin-Friction Drag and Boundary-layer Transition on a Parabolic Body of Revolution (NACA RM-10) at a Mach Number of 1.6 in the Langley 4- by 4-Foot Supersonic Pressure Tunnel. NACA RM L52C24, 1952.

22. Chauvin, Leo T., and Maloney, Joseph P.: Turbulent Convective Heat-Transfer Coefficients Measured From Flight Tests of Four Research Models (NACA RM-10) at Mach Numbers From 1.0 to 3.6. NACA RM L54L15, 1954.

23. McCauley, William D., and Feller, William V.: An Investigation of the Characteristics of the NACA RM-10 (With and Without Fins) in the Langley 11-Inch Hypersonic Tunnel at a Mach Number of 6.9. NACA RM L54I03, 1954

24. Wallskog, Harvey A., and Hart, Roger G.: Investigation of the Drag of Blunt-Nosed Bodies of Revolution in Free Flight at Mach Numbers From 0.6 to 2.3. NACA RM L53D14a, 1953.

25. Jones, Robert T., and Margolis, Kenneth: Flow Over a Slender Body of Revolution at Supersonic Velocities. NACA TN 1081, 1946.

26. Ferri, Antonio: The Linearized Characteristics Method and Its Application to Practical Nonlinear Supersonic Problems. NACA Rep. 1102, 1952. (Supersedes NACA TN 2515.)

27. Ferri, Antonio: Elements of Aerodynamics of Supersonic Flows. The MacMillan Co., 1949.

28. Jones, Robert T.: Thin Oblique Airfoils at Supersonic Speed. NACA Rep. 851, 1946. (Supersedes NACA TN 1107.)

29. De Moraes, Carlos A.: Transonic Flight Test of a Rocket-Powered Model To Determine Propulsive Jet Influence on the Configuration Drag. NACA RM L54D27, 1954.

TABLE I.- LOCATION OF PRESSURE ORIFICES

ON BODY - MODEL A

x, in.	x/L	ϕ, deg
-10.88	-0.074	Static tube
2	.014	45
[a]10	.068	45
19	.130	45
37	.253	45
57	.389	45
77	.526	45
97	.662	45
114	.778	45
123	.840	45
129.5	.884	45
135	.921	15
135	.921	30
135	.921	45
139.5	.952	45
144.5	.986	15
144.5	.986	30
[a]144.5	.986	45
146.2	.998	30
Base	---	--
Nozzle	---	--

[a]The telemeters shorted out at this station.

TABLE II.- LOCATION OF ORIFICES

ON FIN - MODEL A

x/L	X/c	$\frac{y}{b/2}$
0.890	0.033	[a]0.290
.928	.376	[a].278
.959	.650	[a].262
.993	.960	[a].238
.902	.033	[b].355
.940	.376	[b].334
.970	.650	[b].318
1.005	.960	[b].294

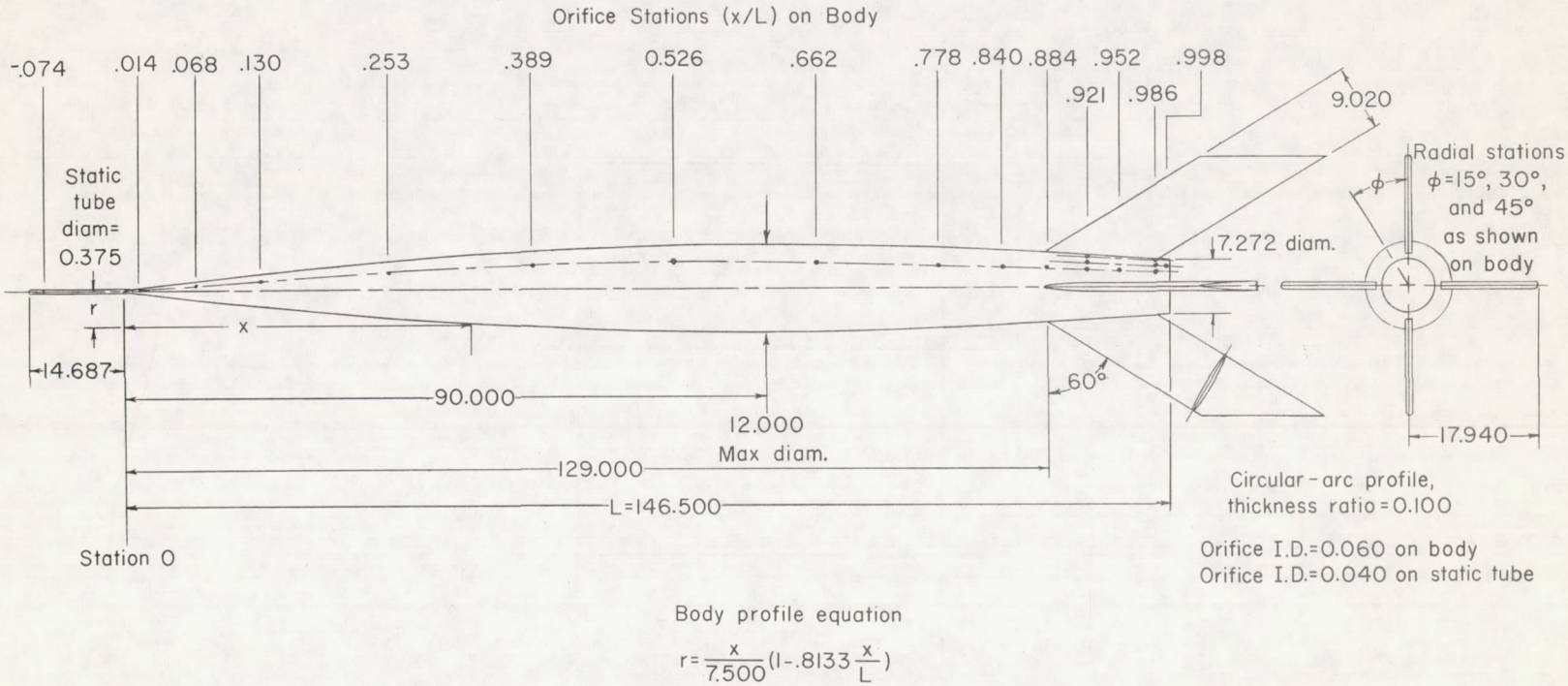
[a] $\left(\frac{y}{b/2}\right)_{av}$ = 0.27 for the orifices located 1 inch from body along constant thickness line of fin.

[b] $\left(\frac{y}{b/2}\right)_{av}$ = 0.33 for the orifices located 3 inches from body along constant thickness line of fin.

TABLE III.- LOCATION OF PRESSURE

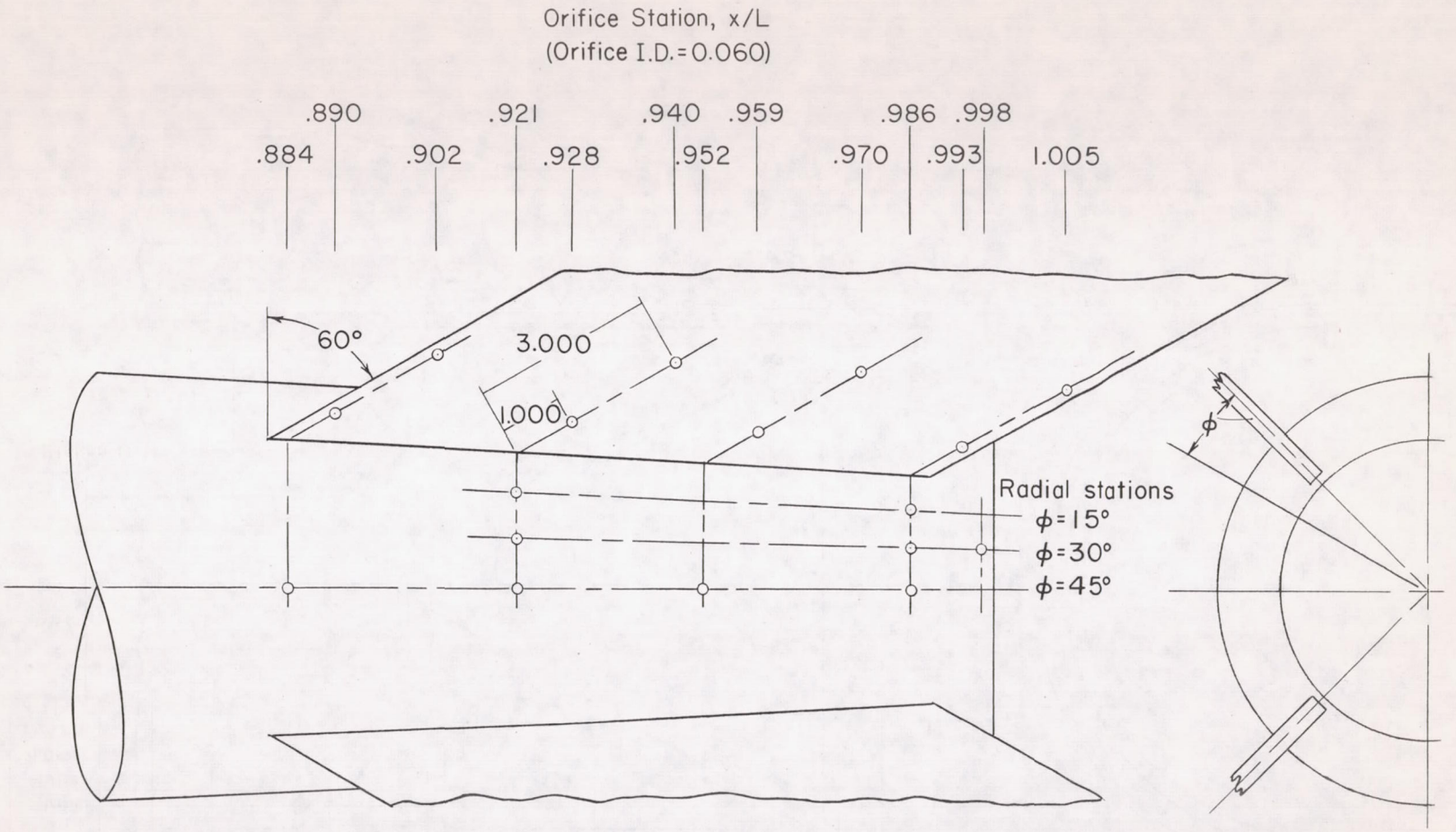
ORIFICES ON BODY - MODEL B

x, in.	x/L	ϕ, deg
129.5	0.884	15
129.5	.884	45
131	.894	15
131	.894	30
131	.894	45
139.5	.952	15
139.5	.952	30
139.5	.952	45
144.5	.986	15
146.2	.998	15
Base	---	--



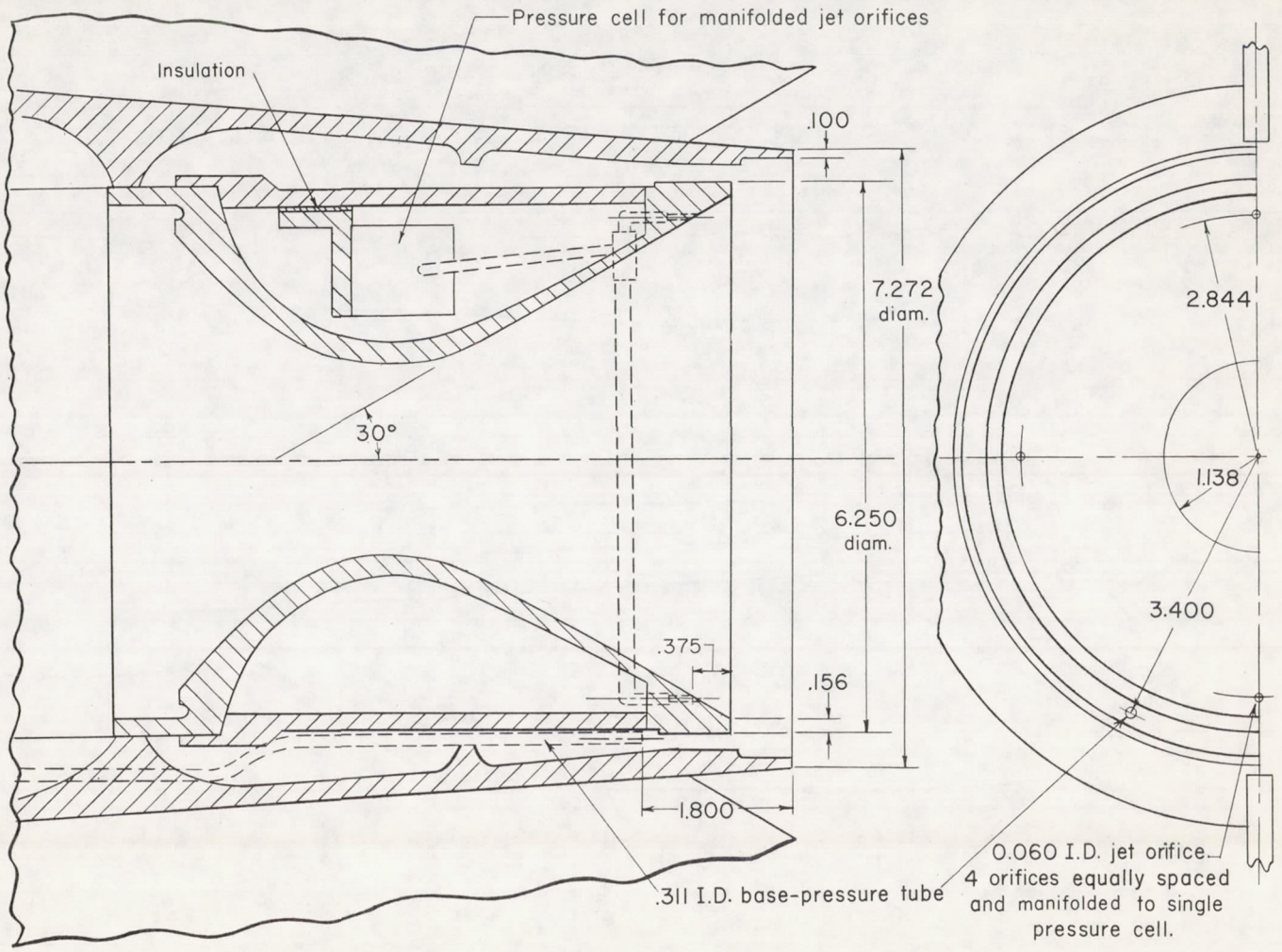
(a) General dimensions and location of pressure orifices on body. Model A.

Figure 1.- Details and dimensions of model A. All dimensions are in inches except where noted.



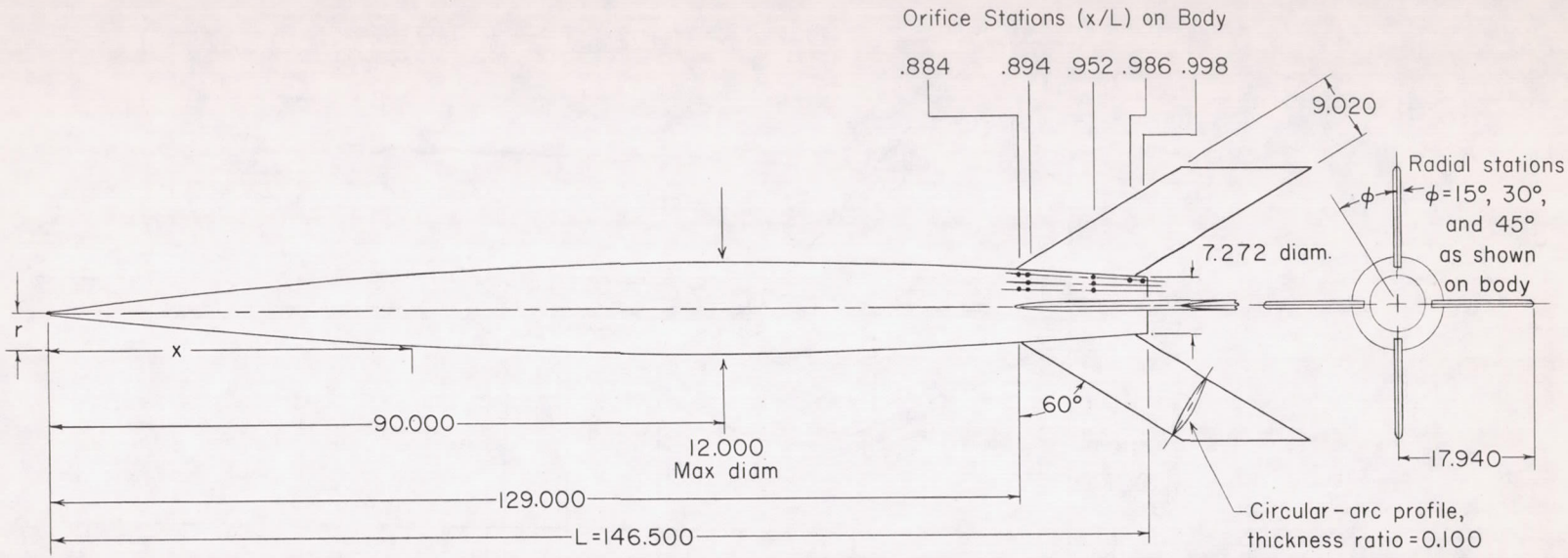
(b) Location of pressure orifices on fin and afterbody. Model A.

Figure 1.- Continued.



(c) Location of jet and base pressure orifices. Model A.

Figure 1.- Concluded.

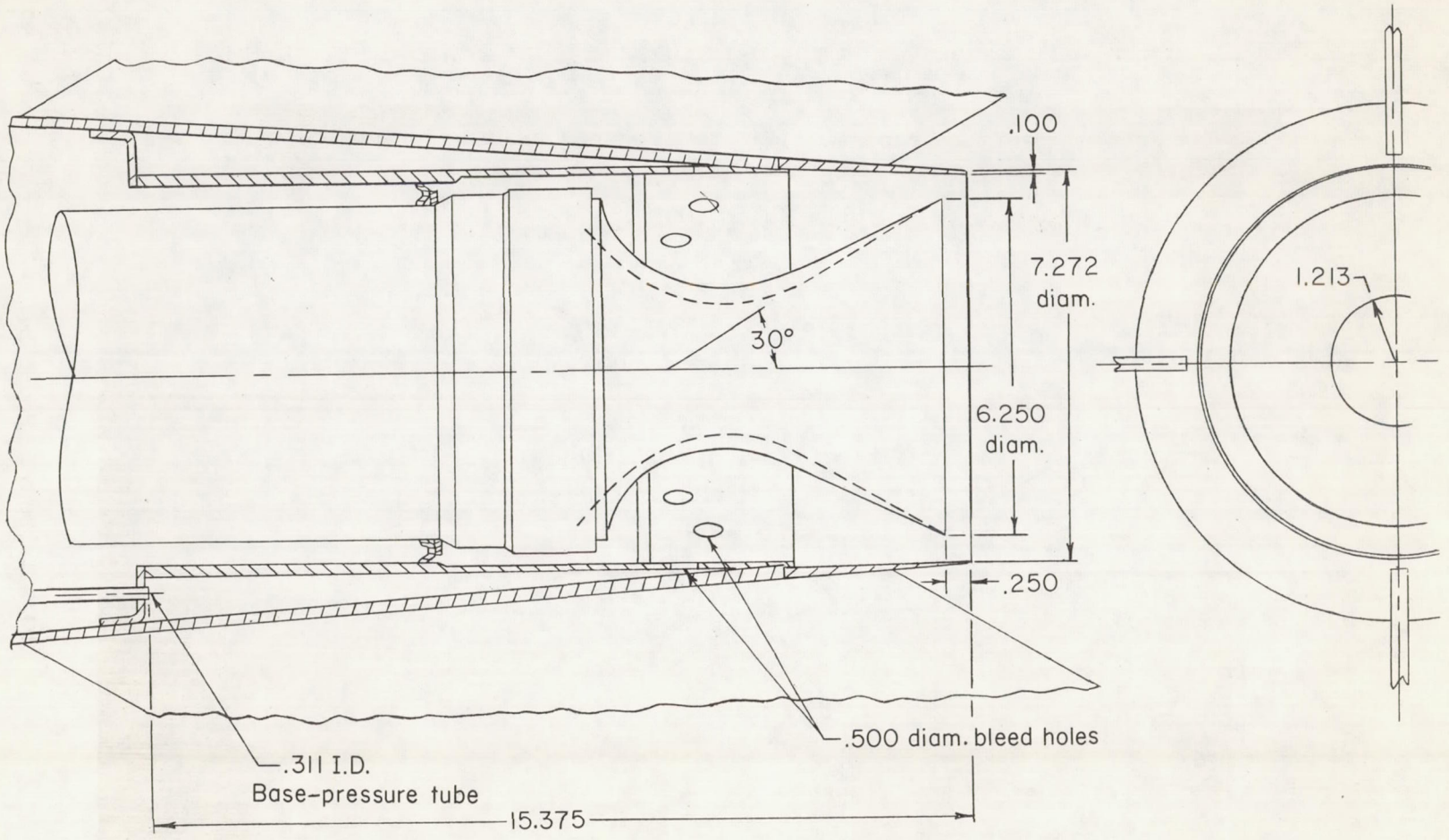


Body profile equation

$$r = \frac{x}{7.500}\left(1 - .8133\frac{x}{L}\right)$$

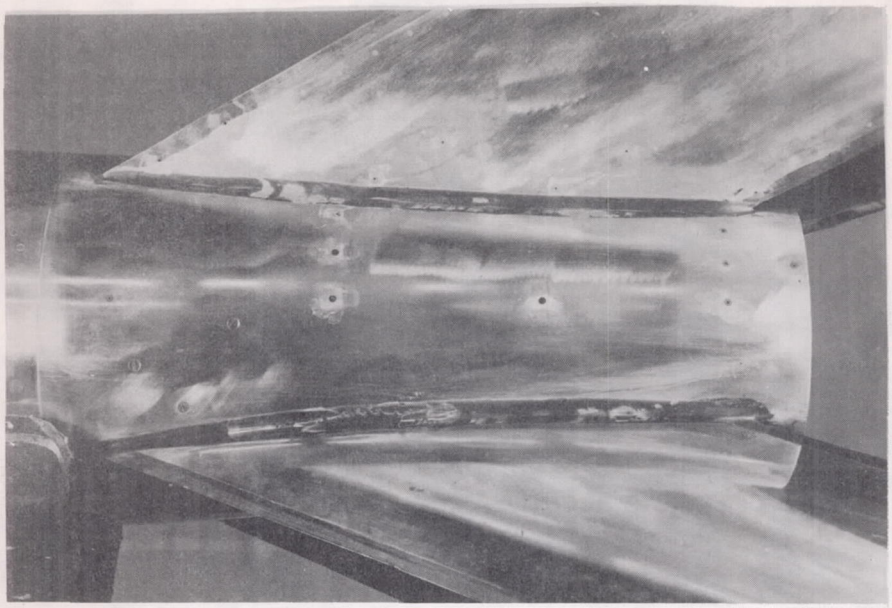
(a) General dimensions and location of pressure orifices on body. Model B.

Figure 2.- Details and dimensions of model B. All dimensions are in inches except where noted.

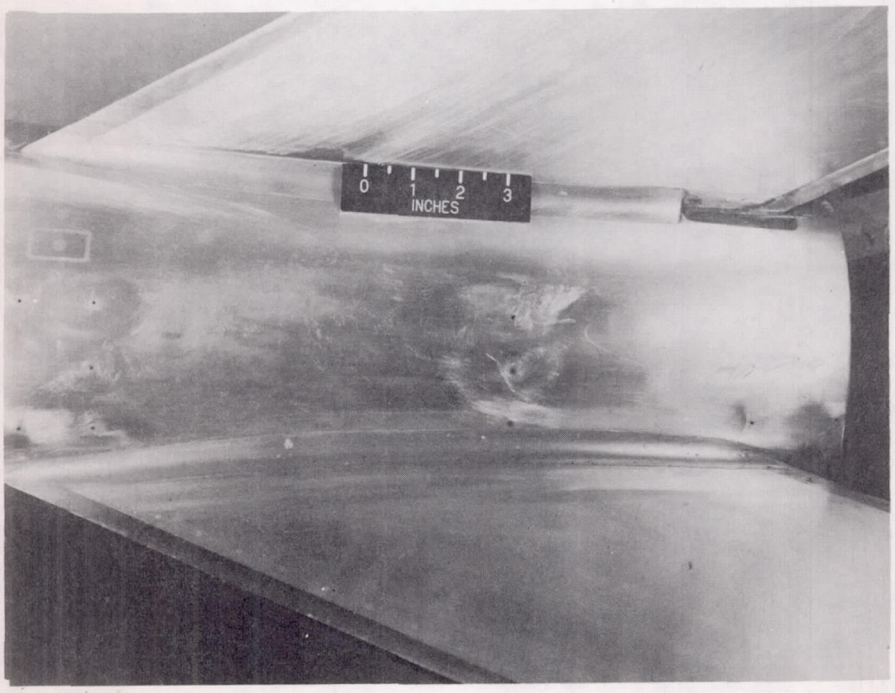


(b) Location of base-pressure orifice. Model B.

Figure 2.- Concluded.

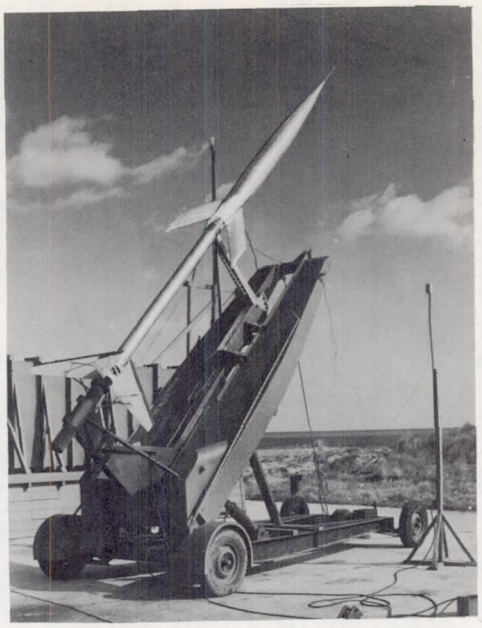


(a) Afterbody. Model A. L-83368



(b) Afterbody. Model B. L-68755

Figure 3.- Photographs of models.



L-83576.1

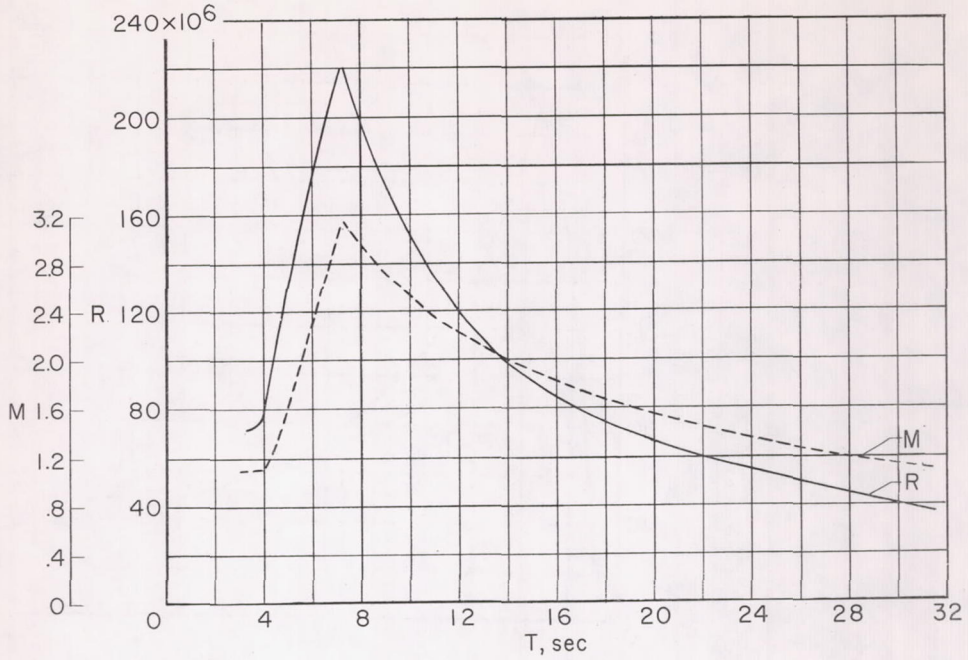
(c) Model A on launcher.



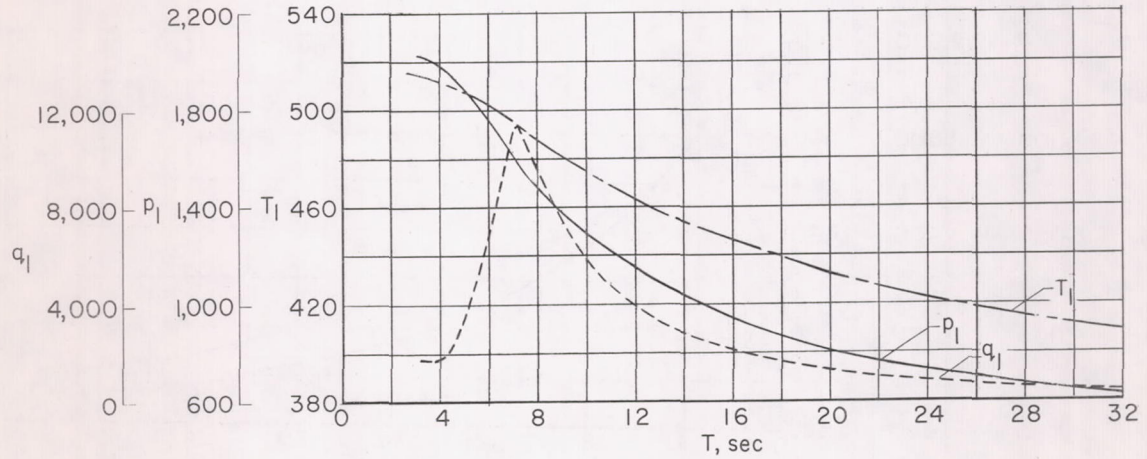
L-68756

(d) Model B on launcher.

Figure 3.- Concluded.

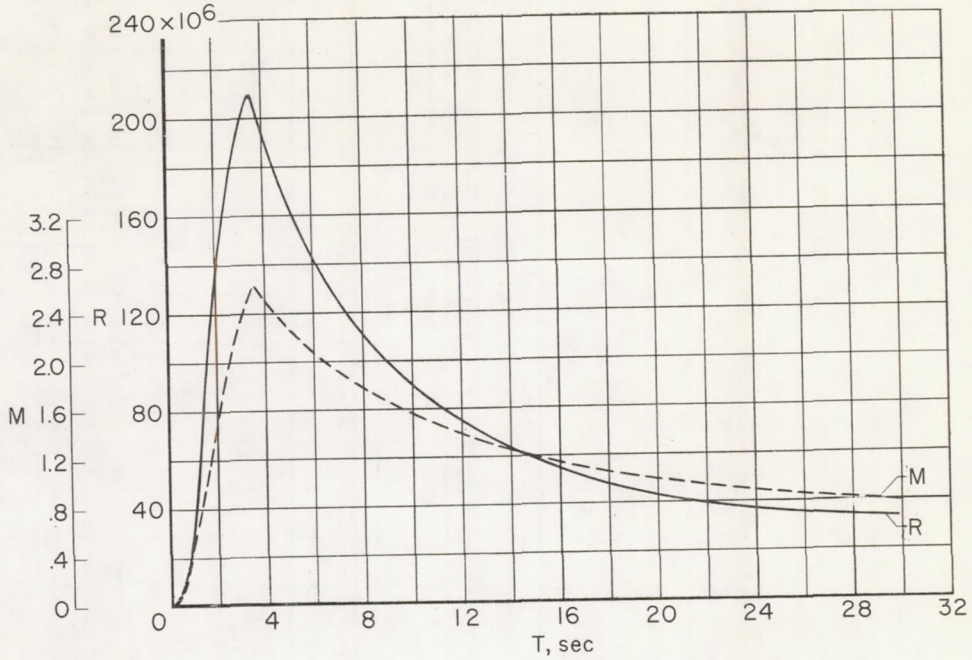


(a) Mach number and Reynolds number. Model A.

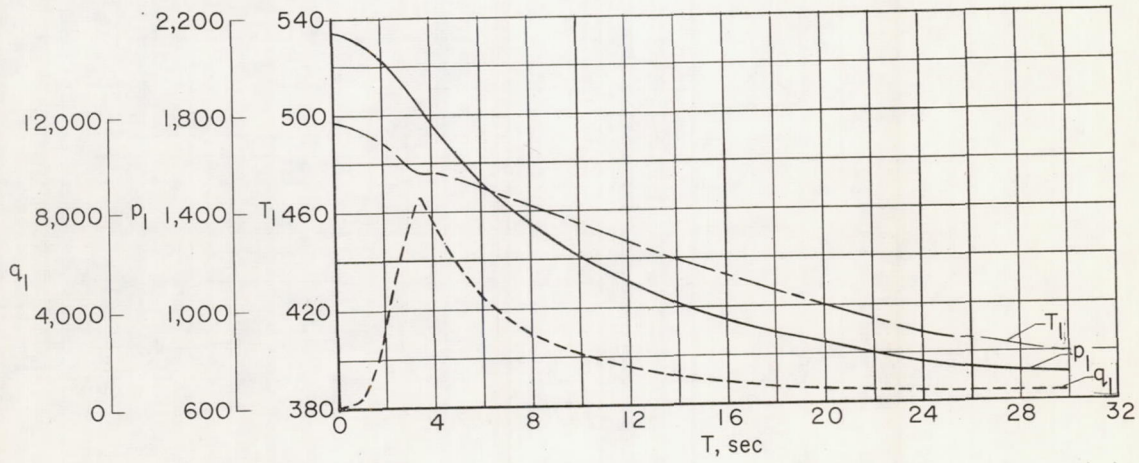


(b) Free-stream conditions. Model A.

Figure 4.- Variations of Mach number, Reynolds number, and free-stream conditions with time for models tested.



(c) Mach number and Reynolds number. Model B.



(d) Free-stream conditions. Model B.

Figure 4.- Concluded.

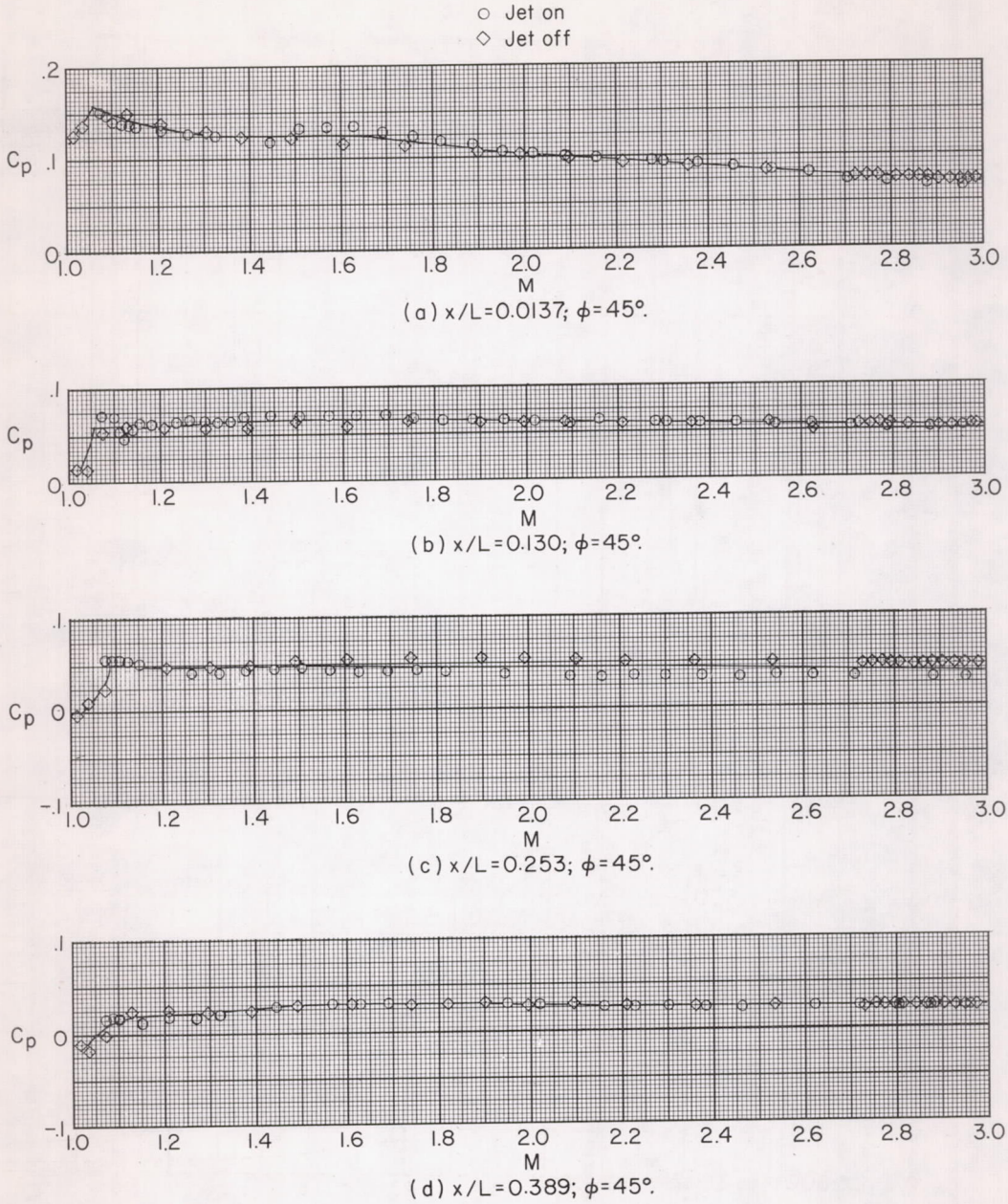


Figure 5.- Variations of the body, base, and nozzle pressure coefficients with Mach number for model A.

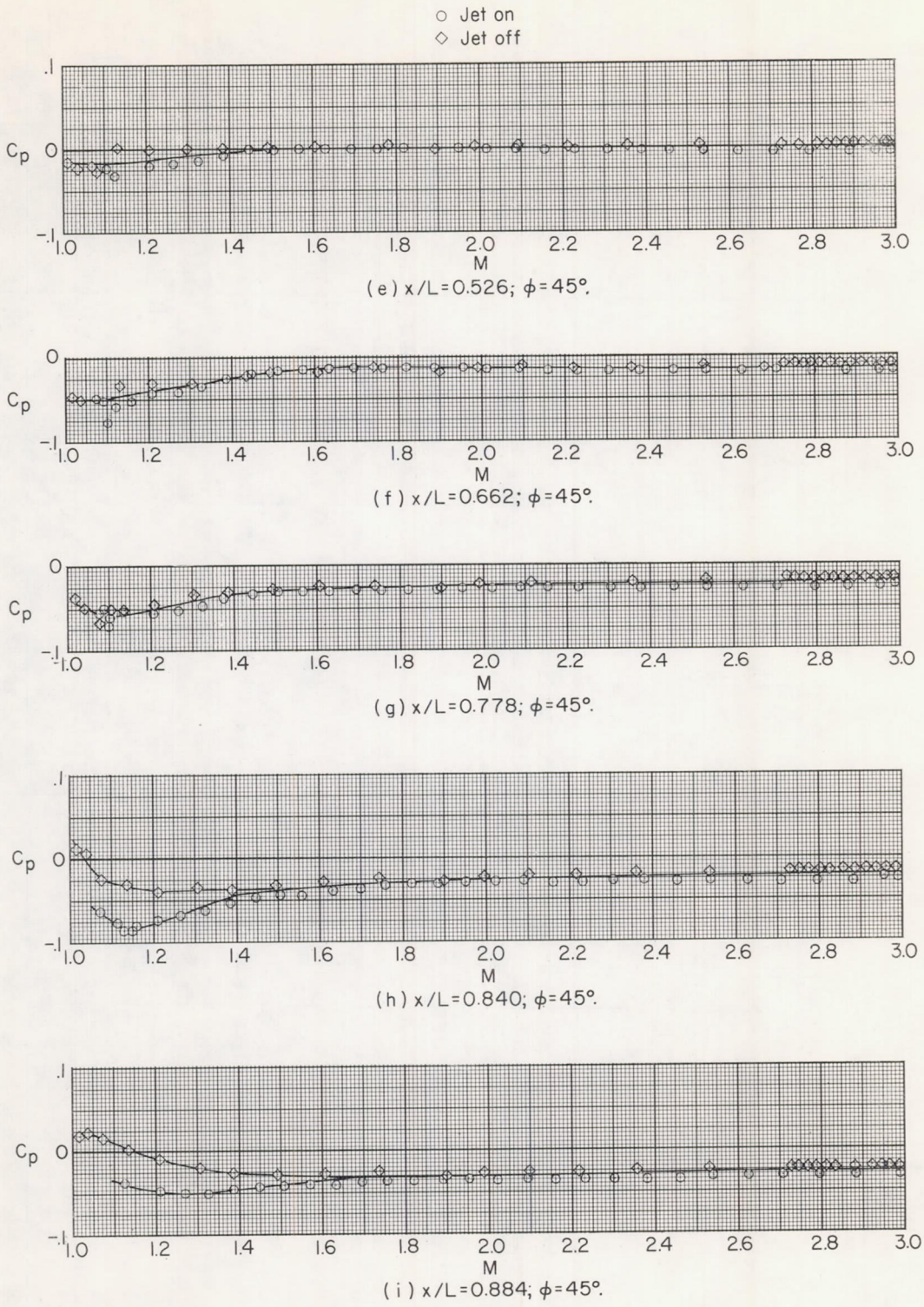


Figure 5.- Continued.

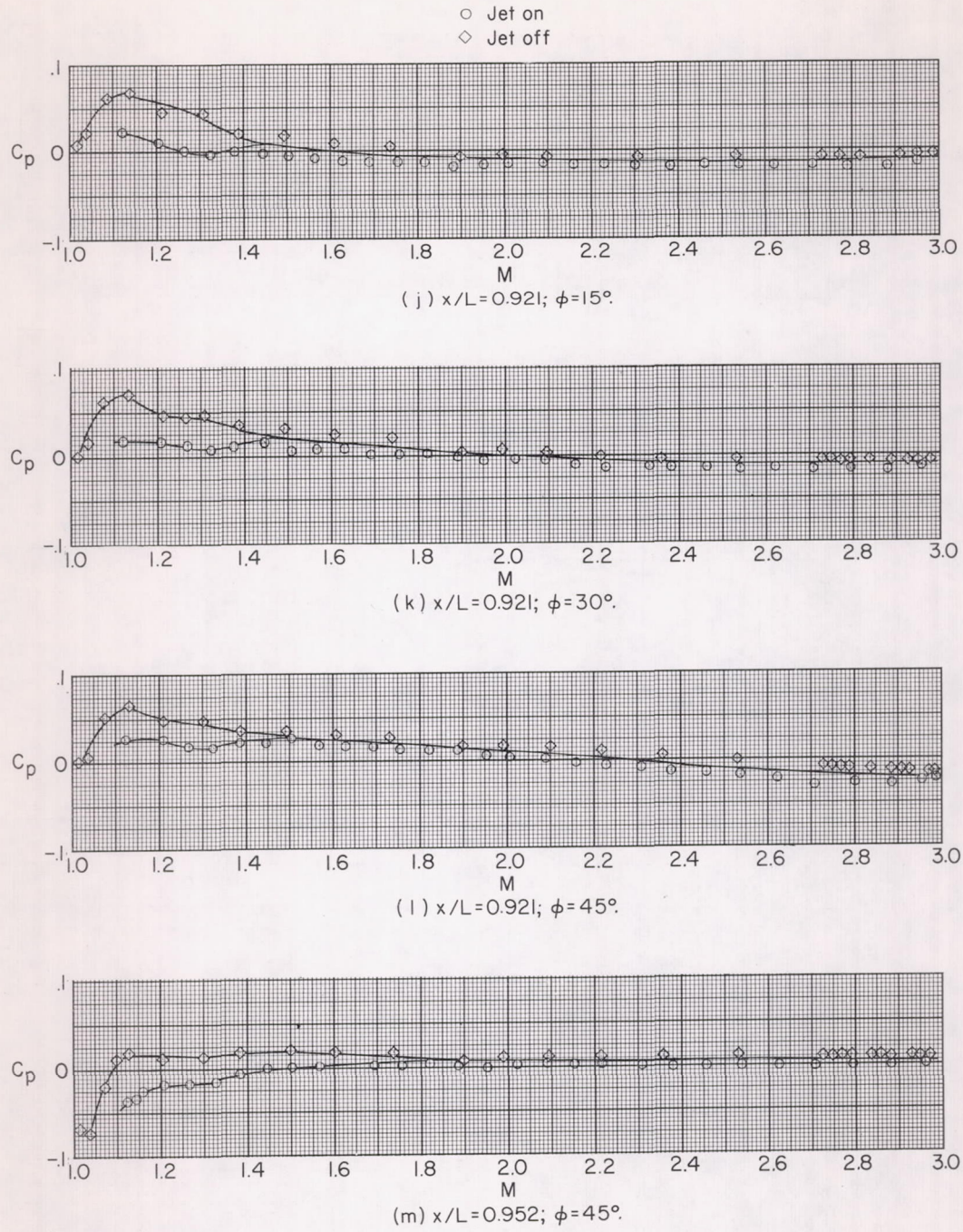
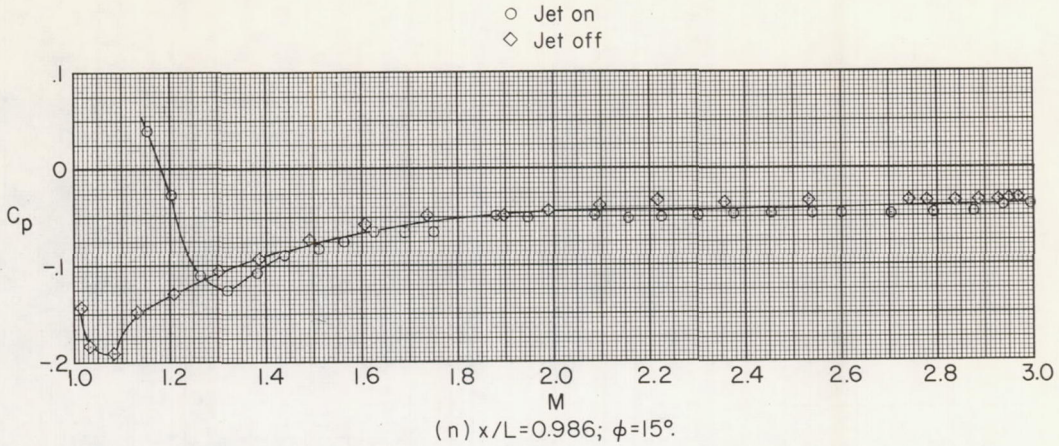


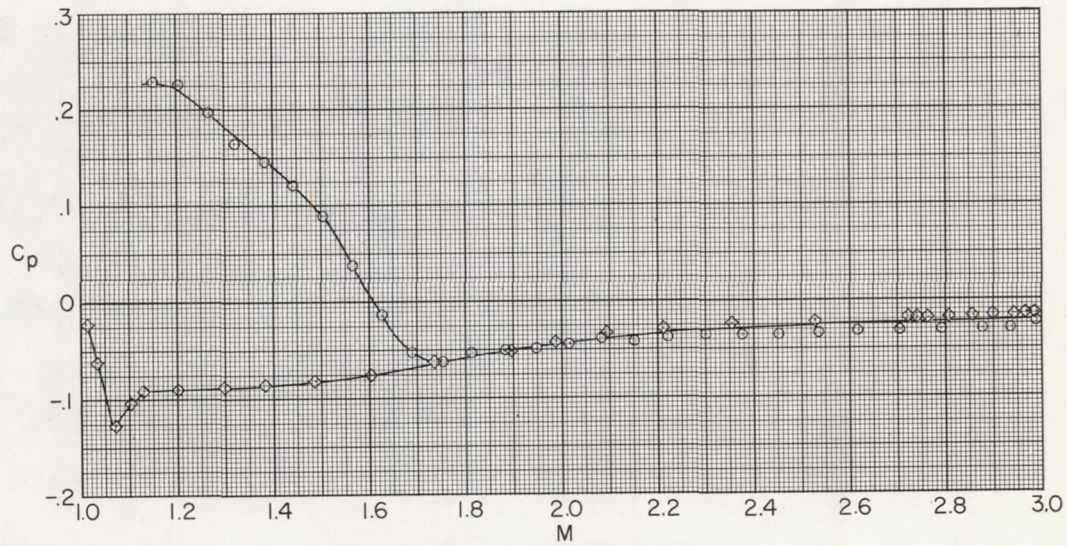
Figure 5.- Continued.



(n) x/L=0.986; ϕ=15°.

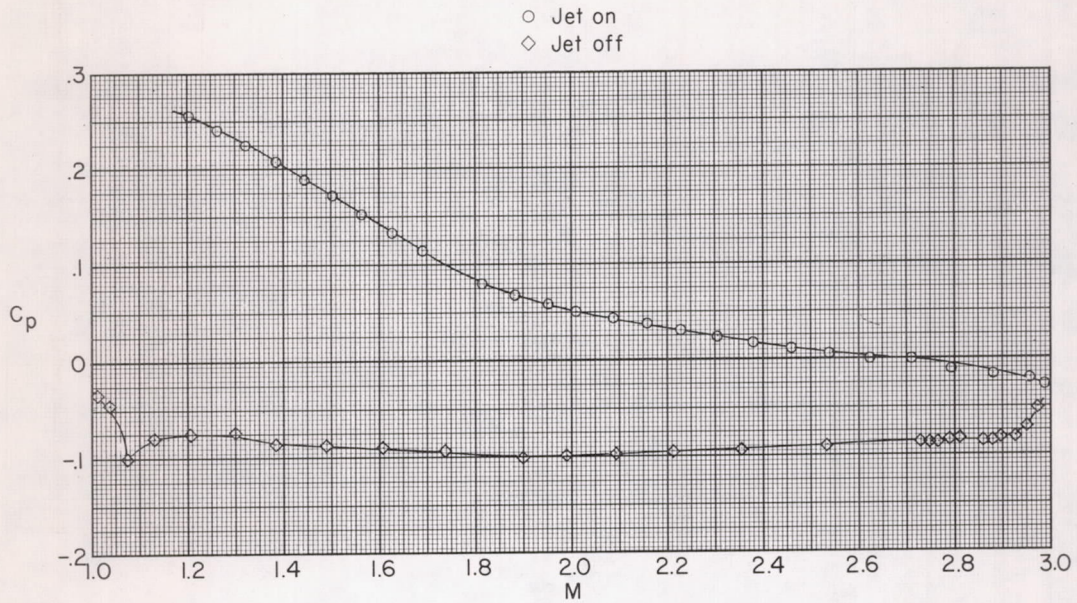


(o) x/L=0.986; ϕ=30°.

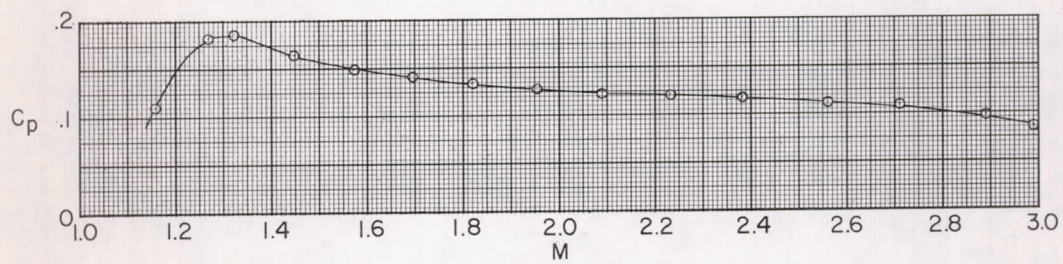


(p) x/L=0.998; ϕ=30°.

Figure 5.- Continued.



(q) Base pressure.



(r) Nozzle pressure.

Figure 5.- Concluded.

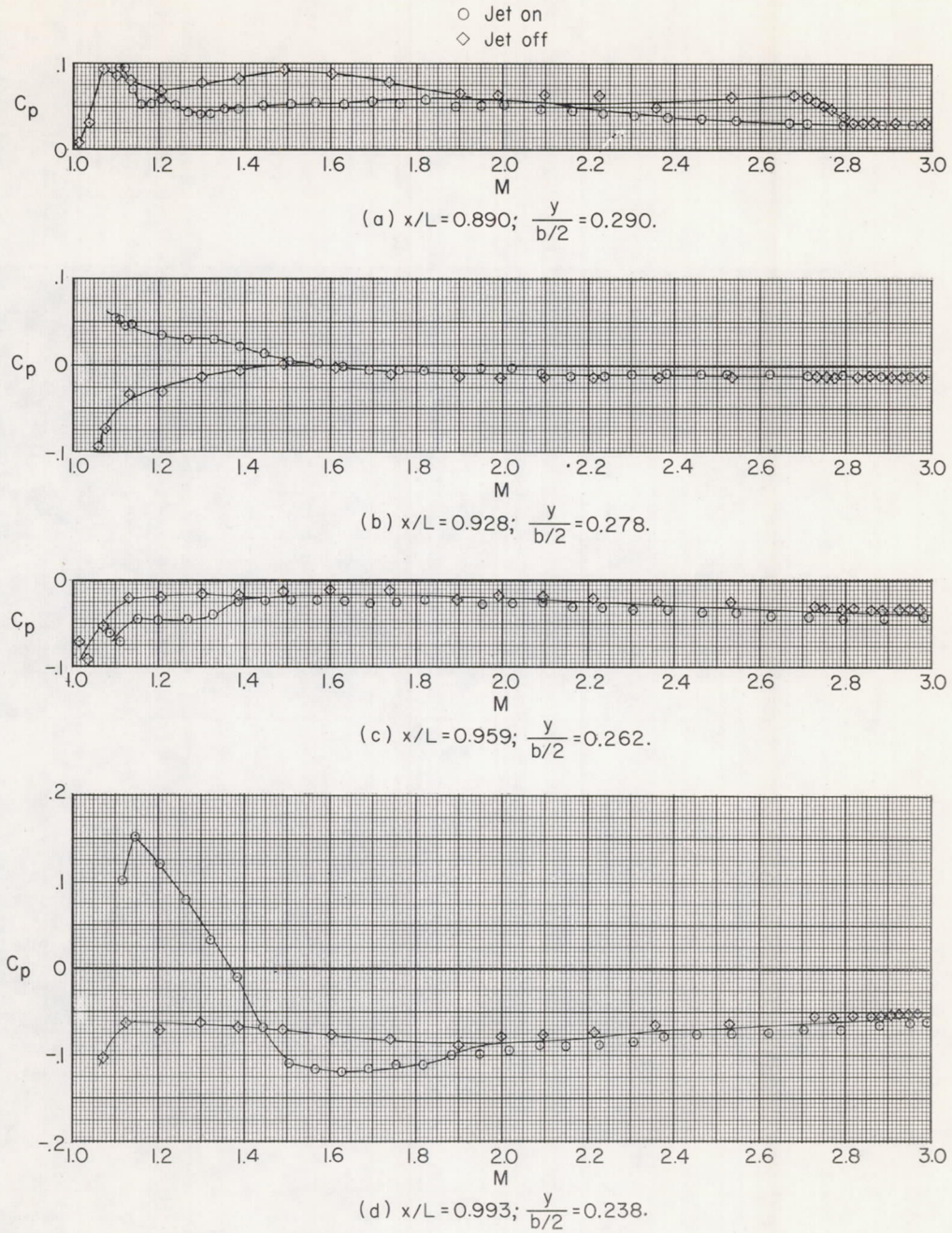
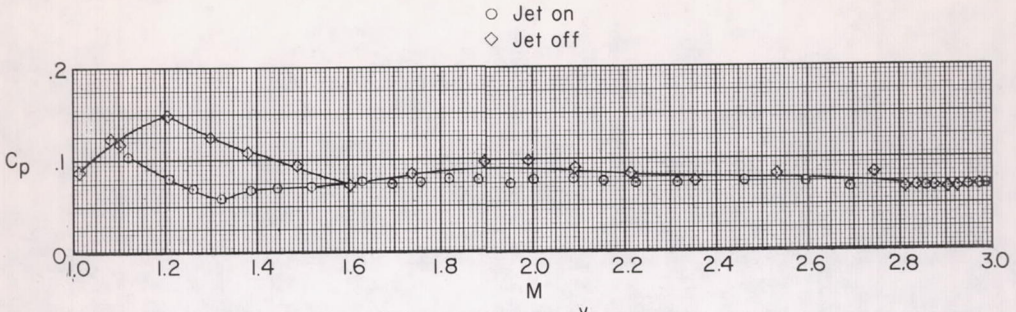
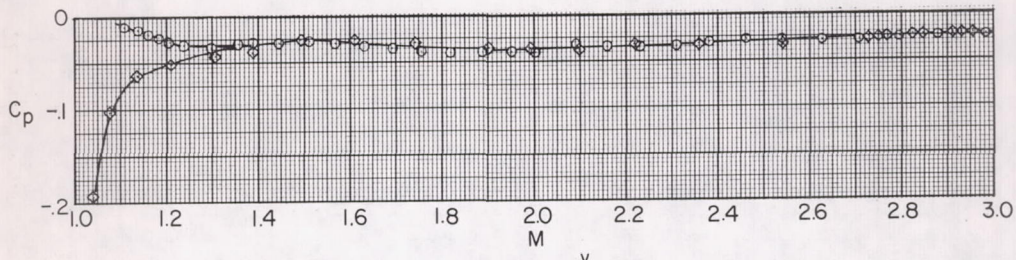


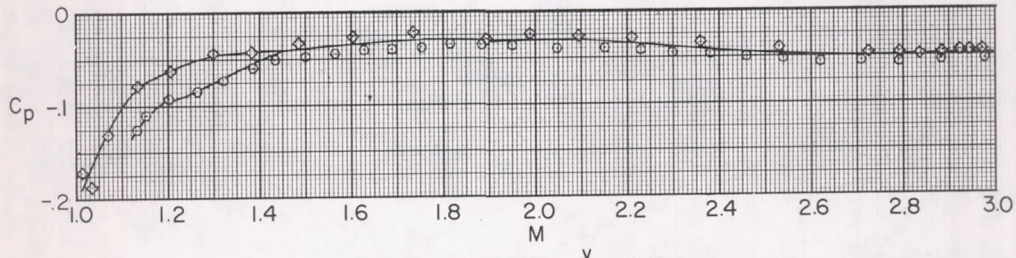
Figure 6.- Variations of the fin pressure coefficients with Mach number for model A.



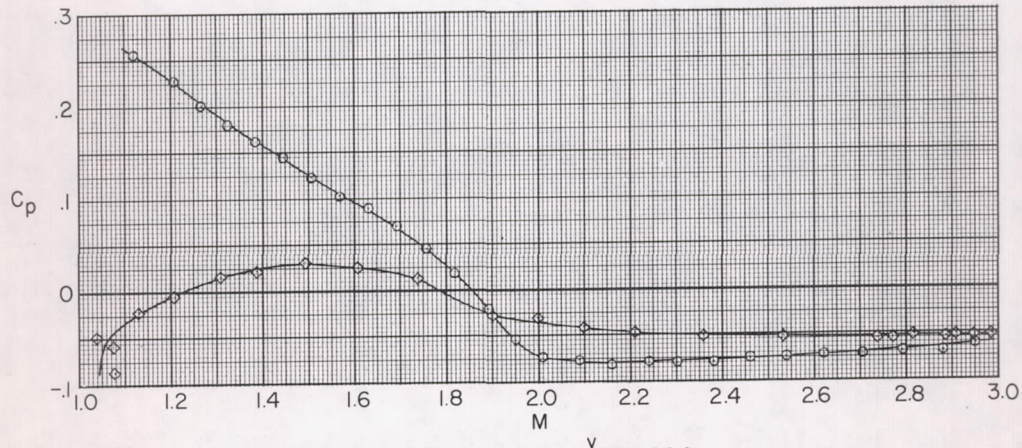
(e) $x/L = 0.902$; $\frac{y}{b/2} = 0.355$.



(f) $x/L = 0.940$; $\frac{y}{b/2} = 0.334$.



(g) $x/L = 0.970$; $\frac{y}{b/2} = 0.318$.



(h) $x/L = 1.005$; $\frac{y}{b/2} = 0.294$.

Figure 6.- Concluded.

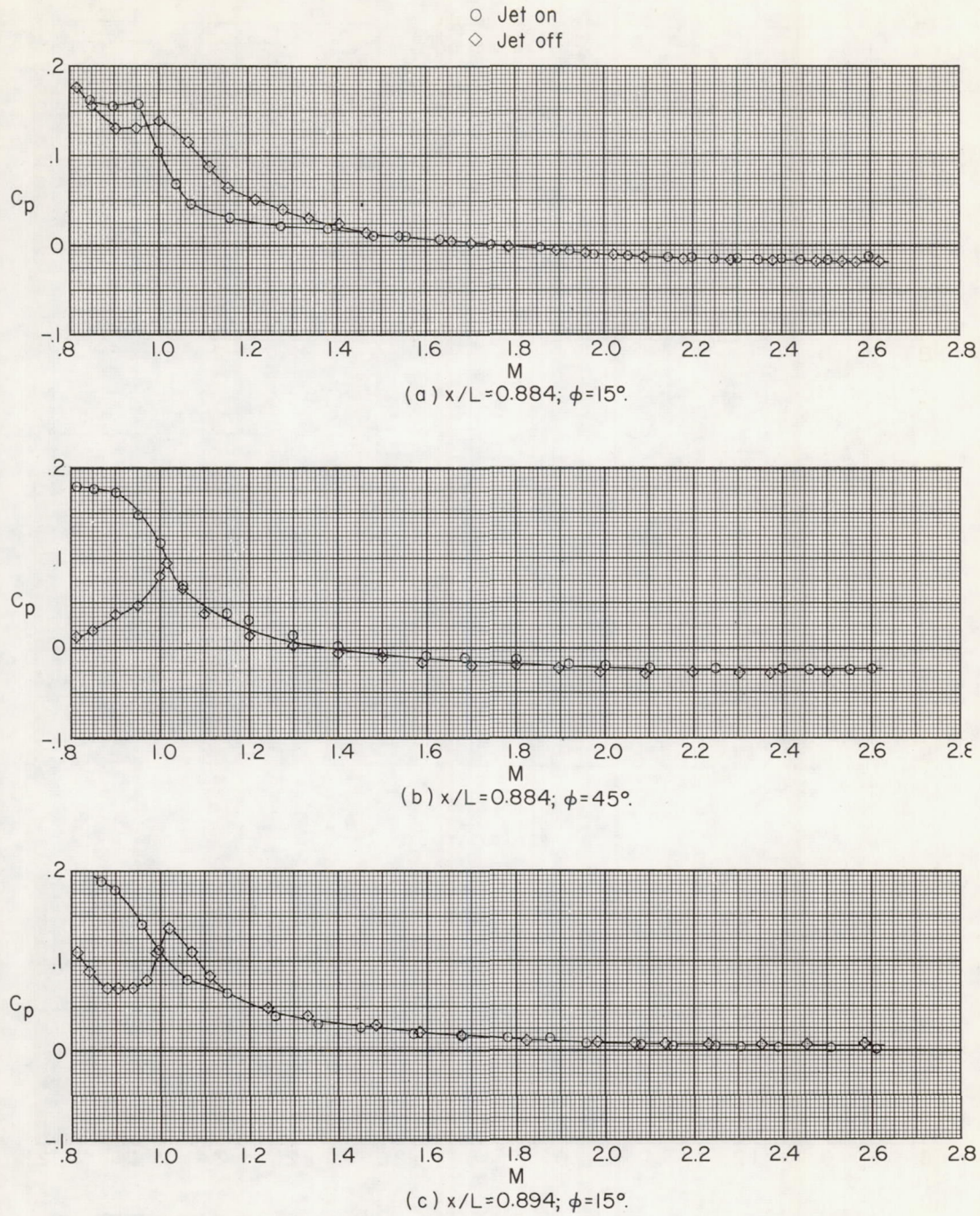
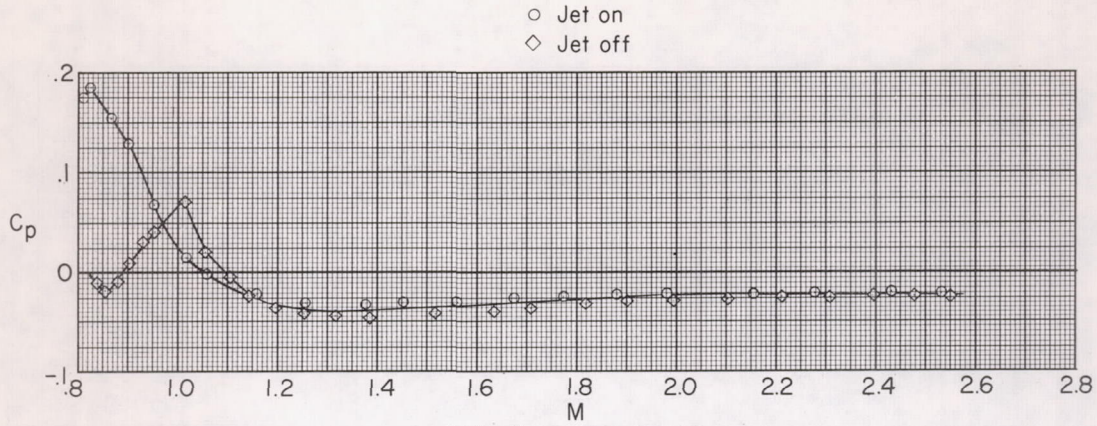
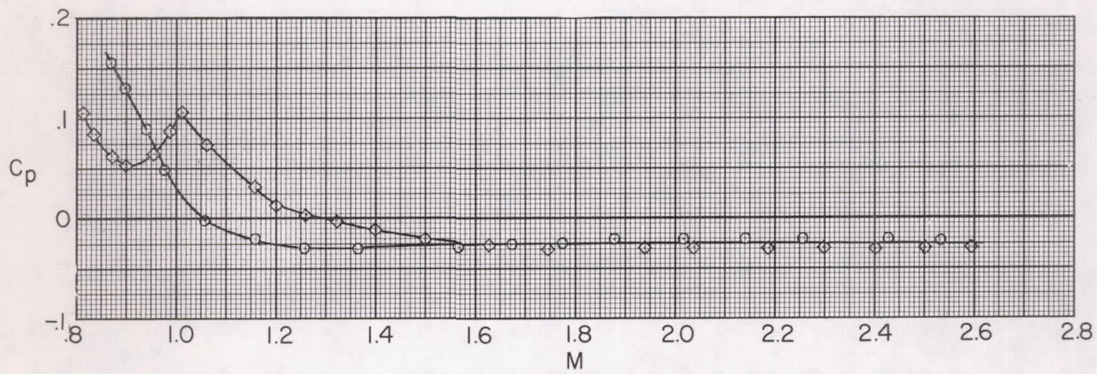


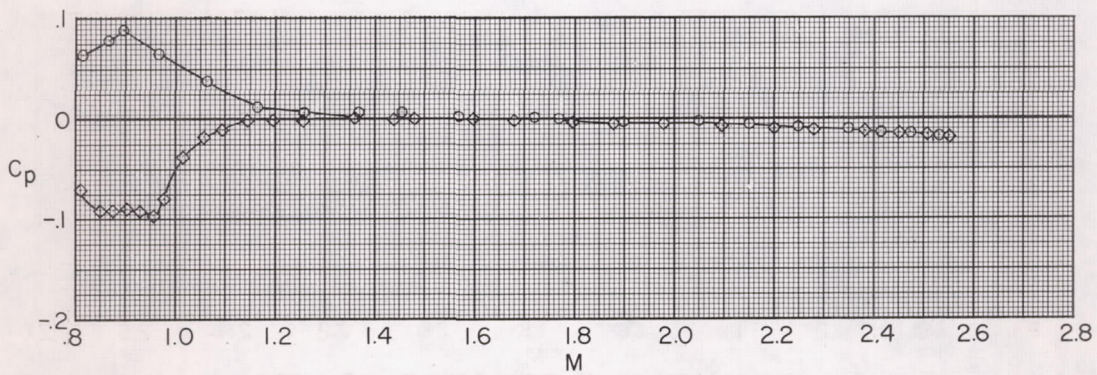
Figure 7.- Variations of the body- and base-pressure coefficients with Mach number for model B.



(d) x/L=0.894; ϕ=30°.

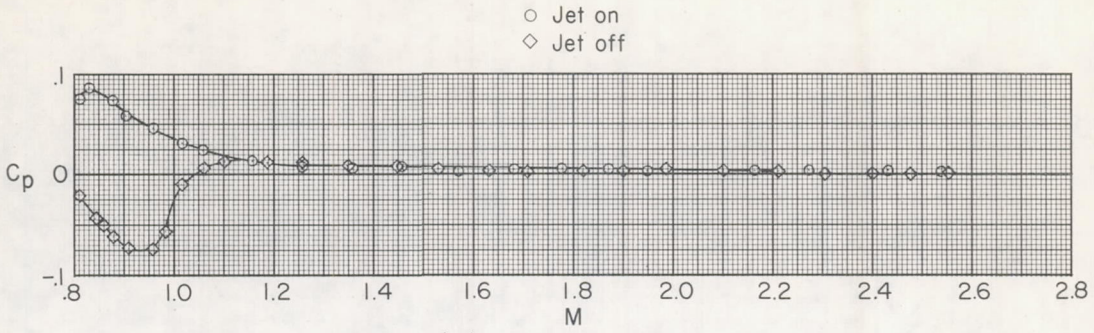


(e) x/L=0.894; ϕ=45°.



(f) x/L=0.952; ϕ=15°.

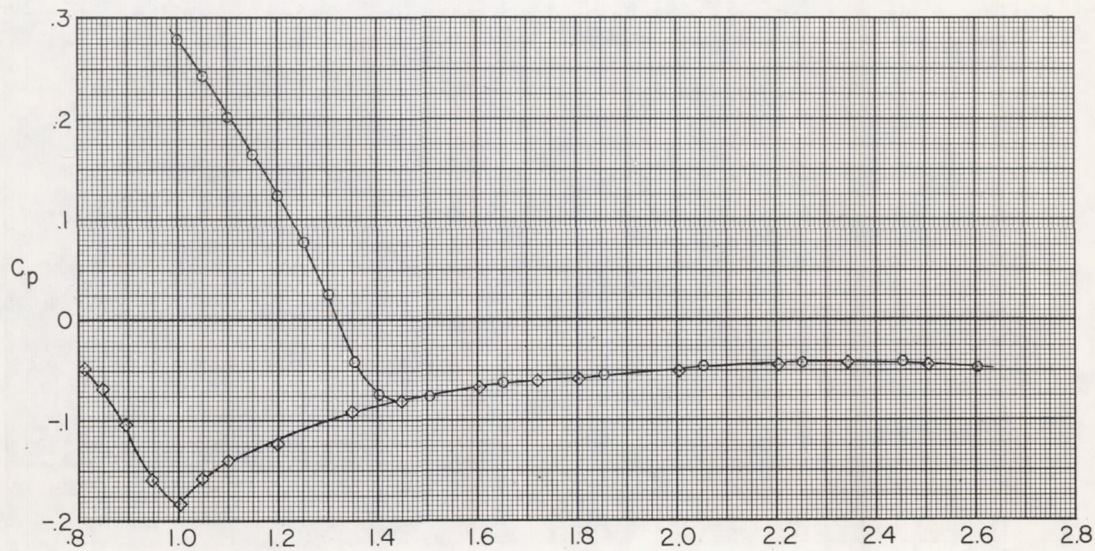
Figure 7.- Continued.



(g) x/L=0.952; ϕ=30°.

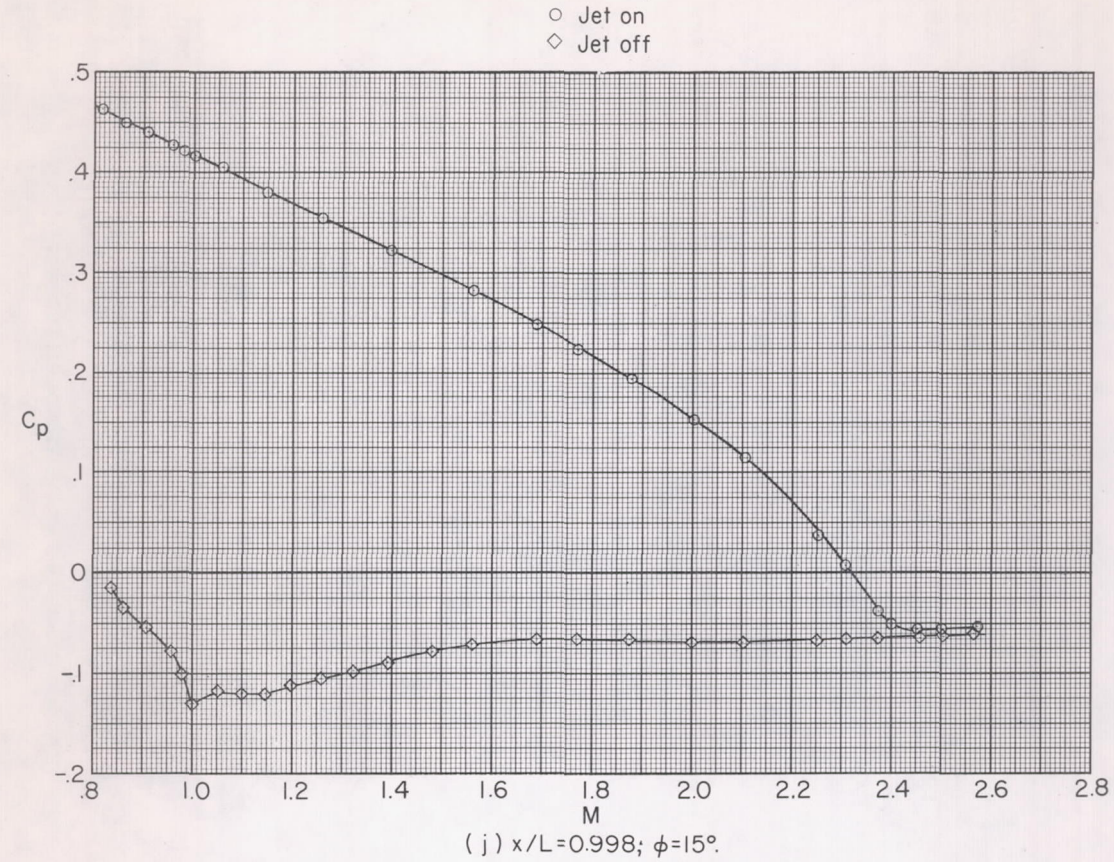


(h) x/L=0.952; ϕ=45°.

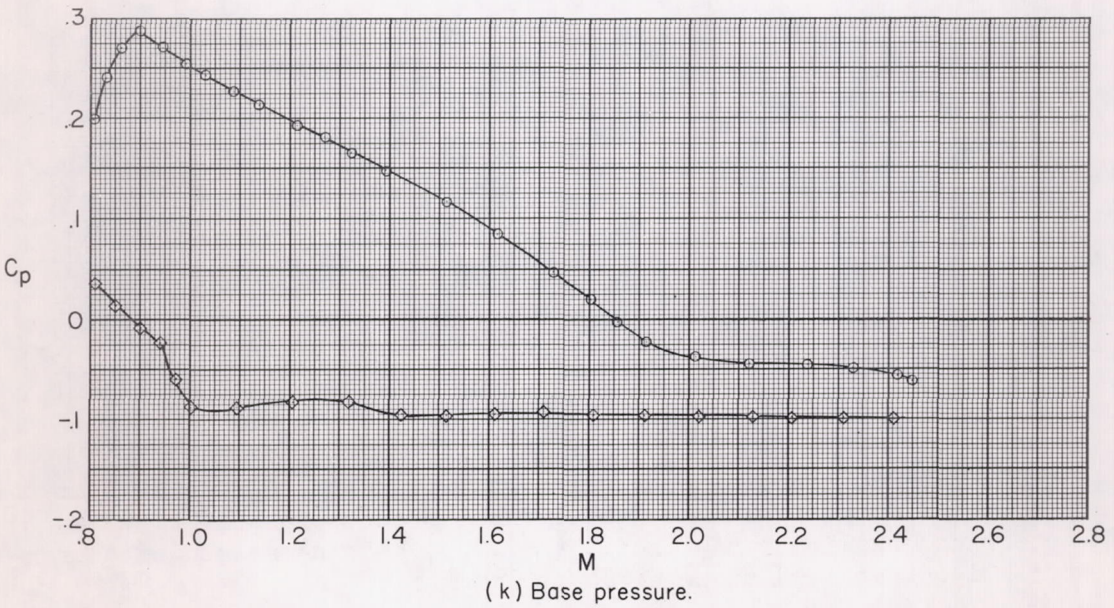


(i) x/L=0.986; ϕ=15°.

Figure 7.- Continued.



(j) x/L=0.998; ϕ=15°.



(k) Base pressure.

Figure 7.- Concluded.

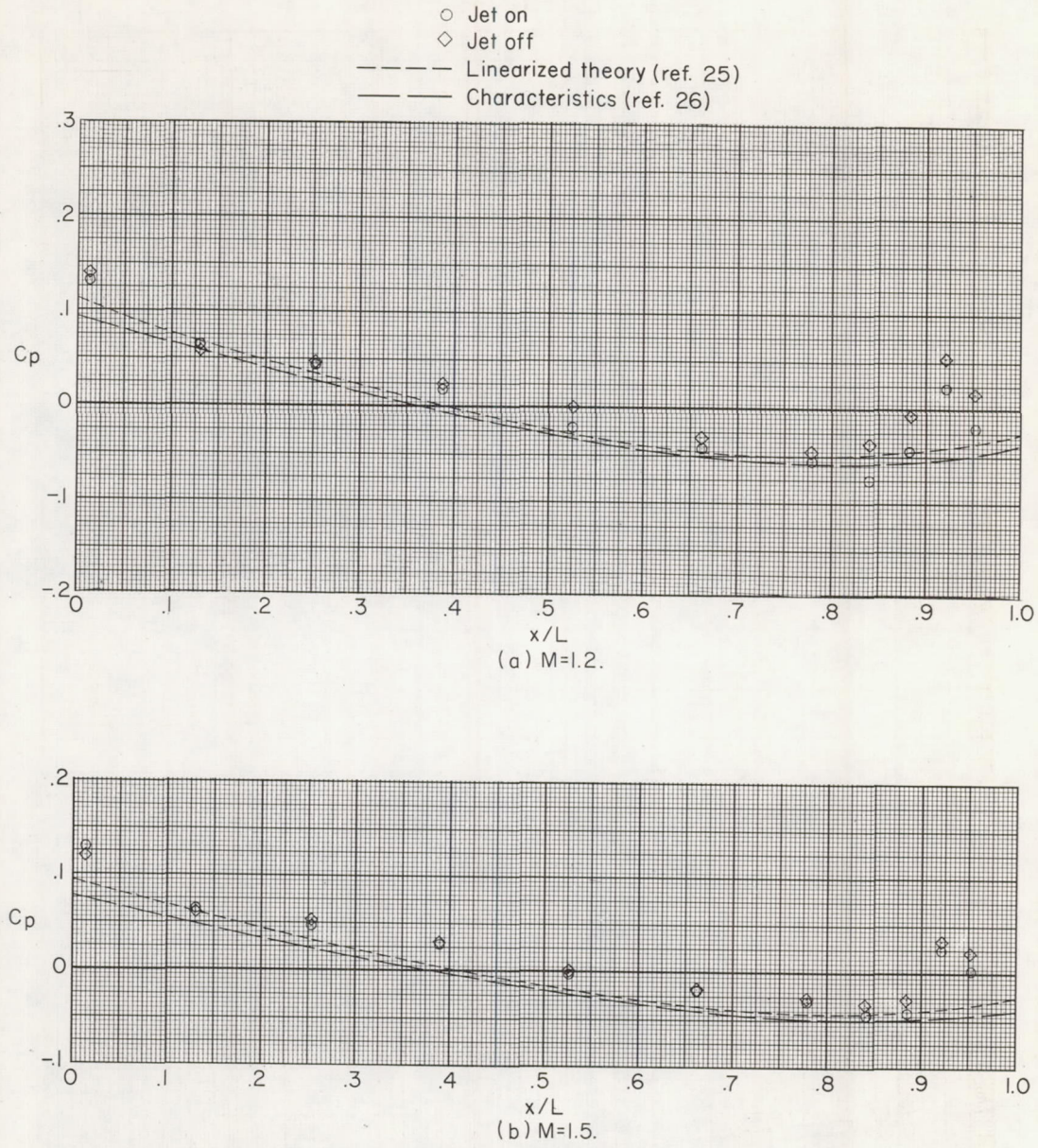


Figure 8.- Comparison of the measured body pressure coefficients at $\phi = 45^{\circ}$ of model A with the theoretical pressure coefficients as determined by linearized theory (ref. 25) and the method of characteristics (ref. 26) at several Mach numbers.

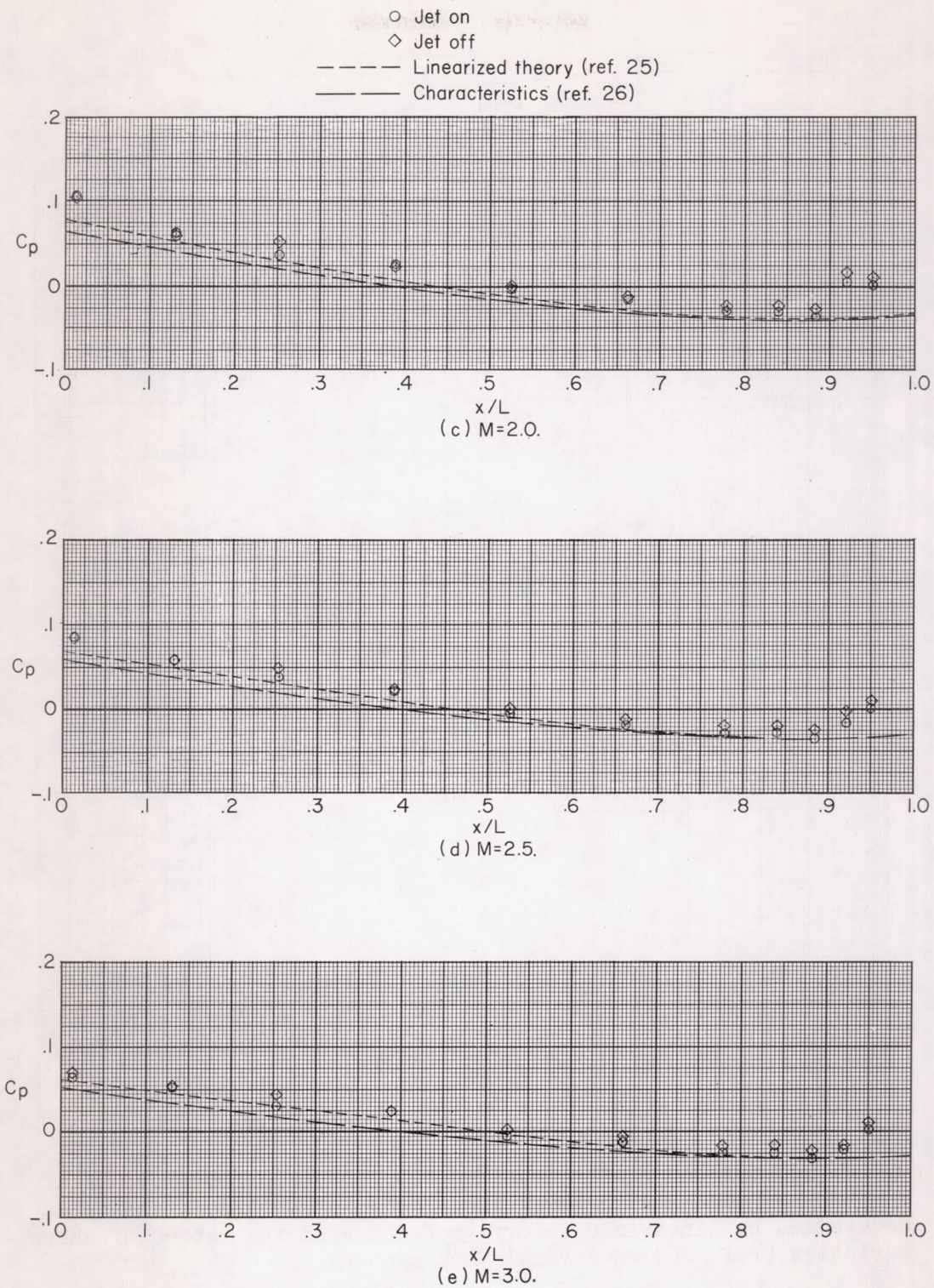
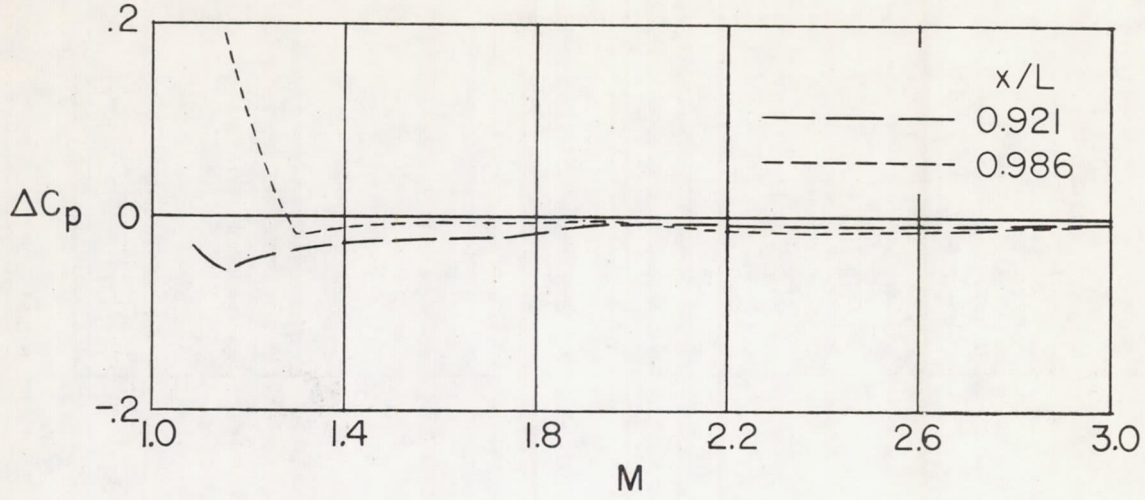
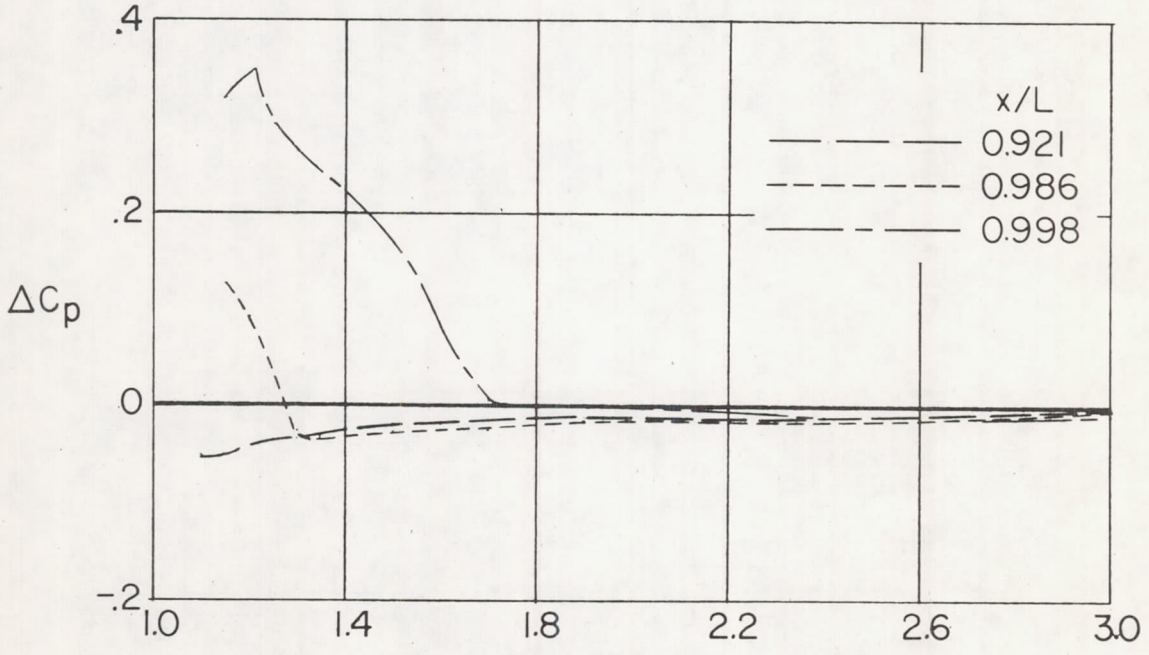


Figure 8.- Concluded.

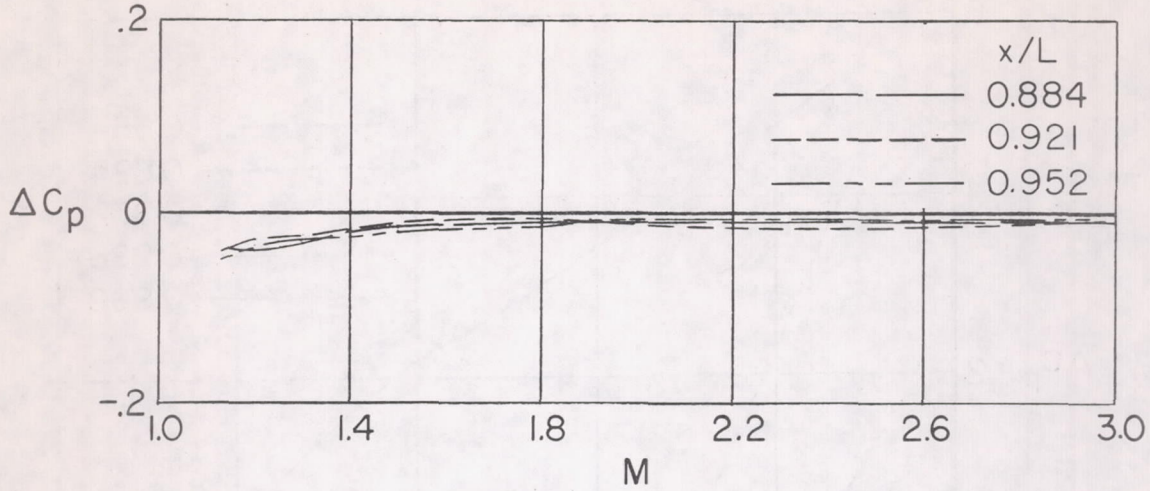


(a) ϕ=15°.

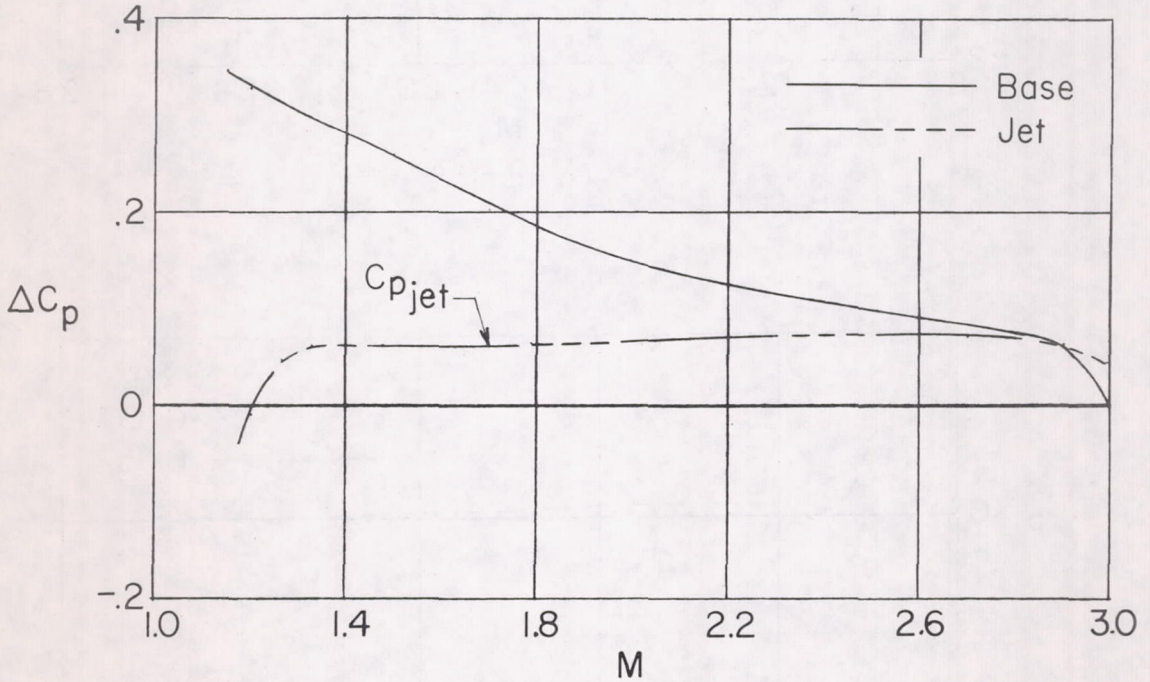


(b) ϕ=30°.

Figure 9.- Comparisons of jet effects at rear body stations of model A.

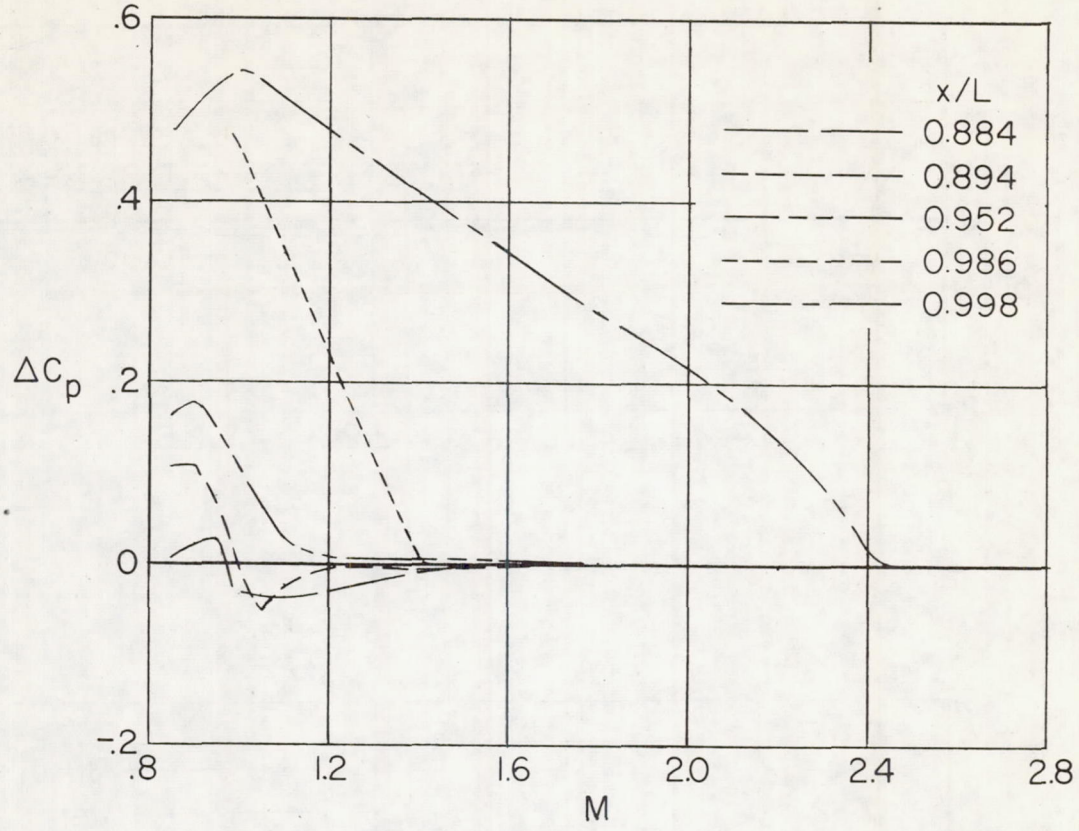


(c) $\phi = 45°$.

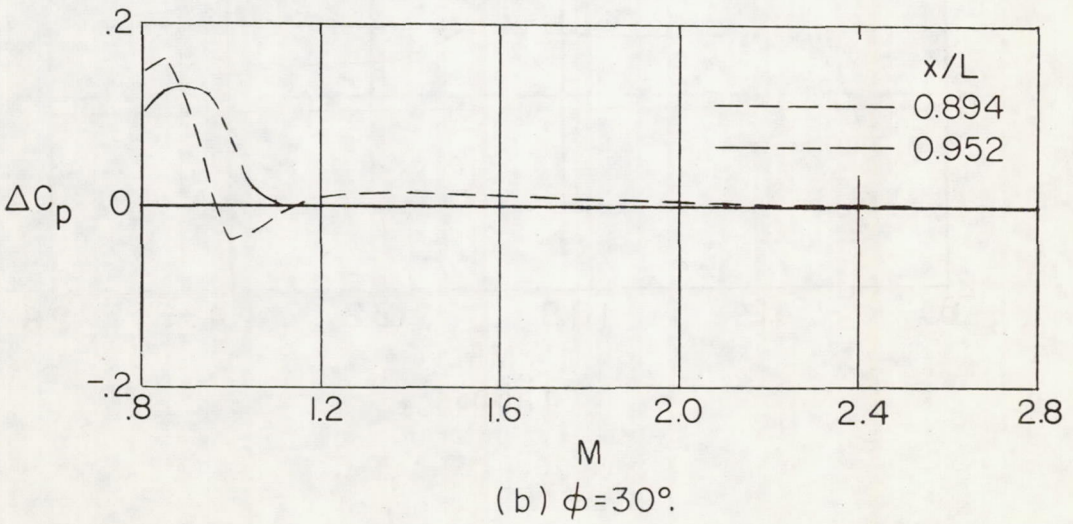


(d) Base.

Figure 9.- Concluded.

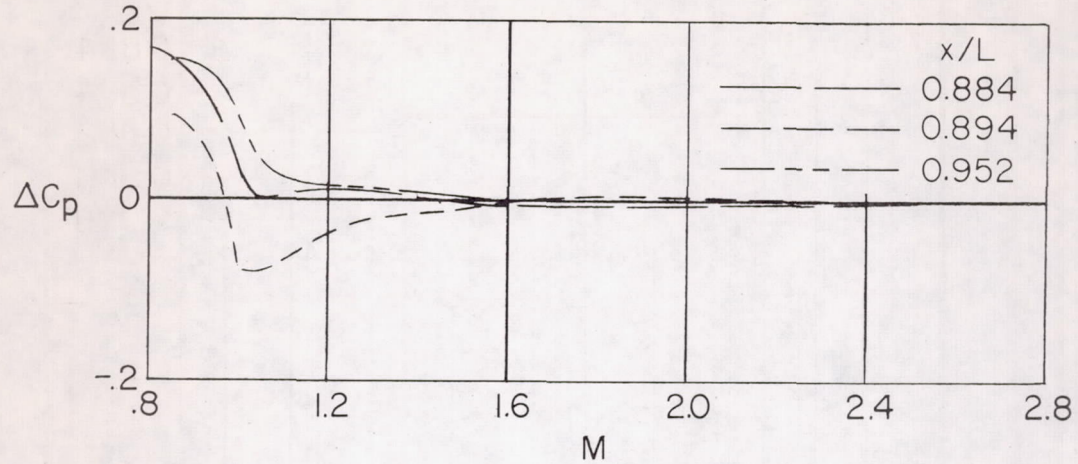


(a) ϕ=15°.

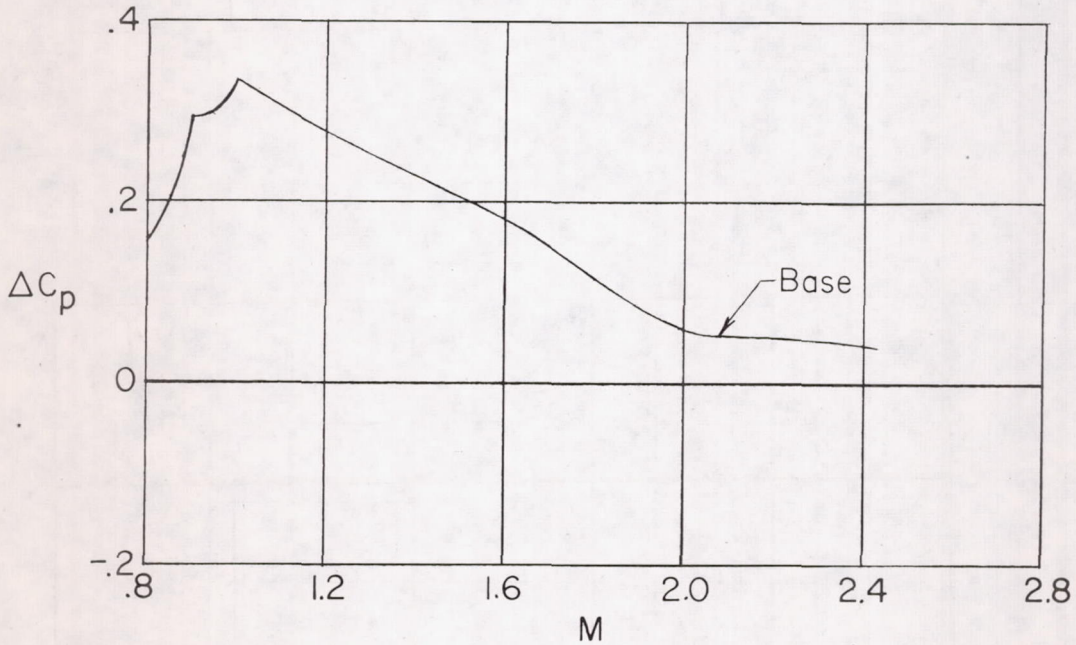


(b) ϕ=30°.

Figure 10.- Comparisons of jet effects at rear body stations of model B.



(c) $\phi = 45°$.



(d) Base.

Figure 10.- Concluded.

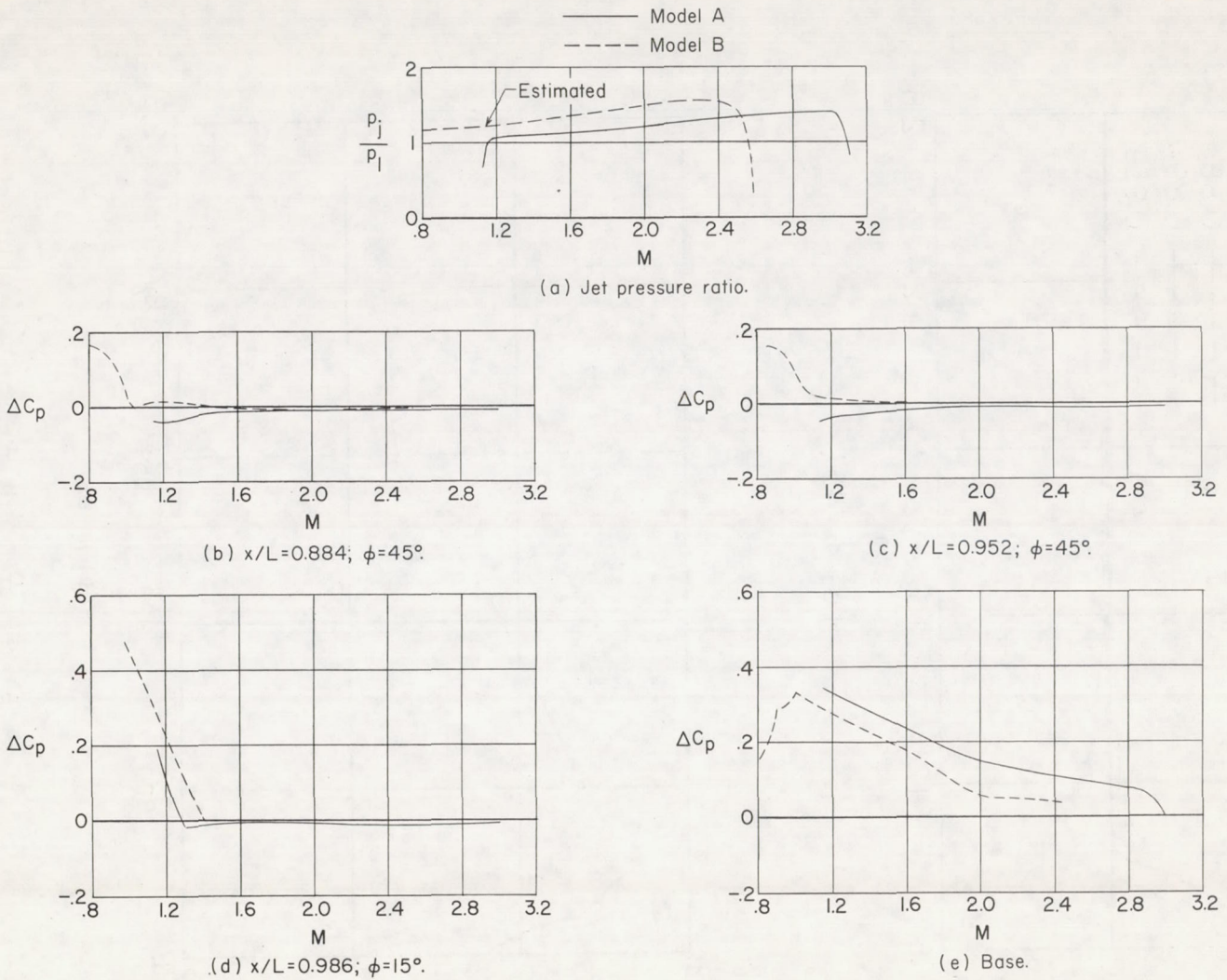


Figure 11.- Comparisons of jet effects at corresponding stations of models A and B.

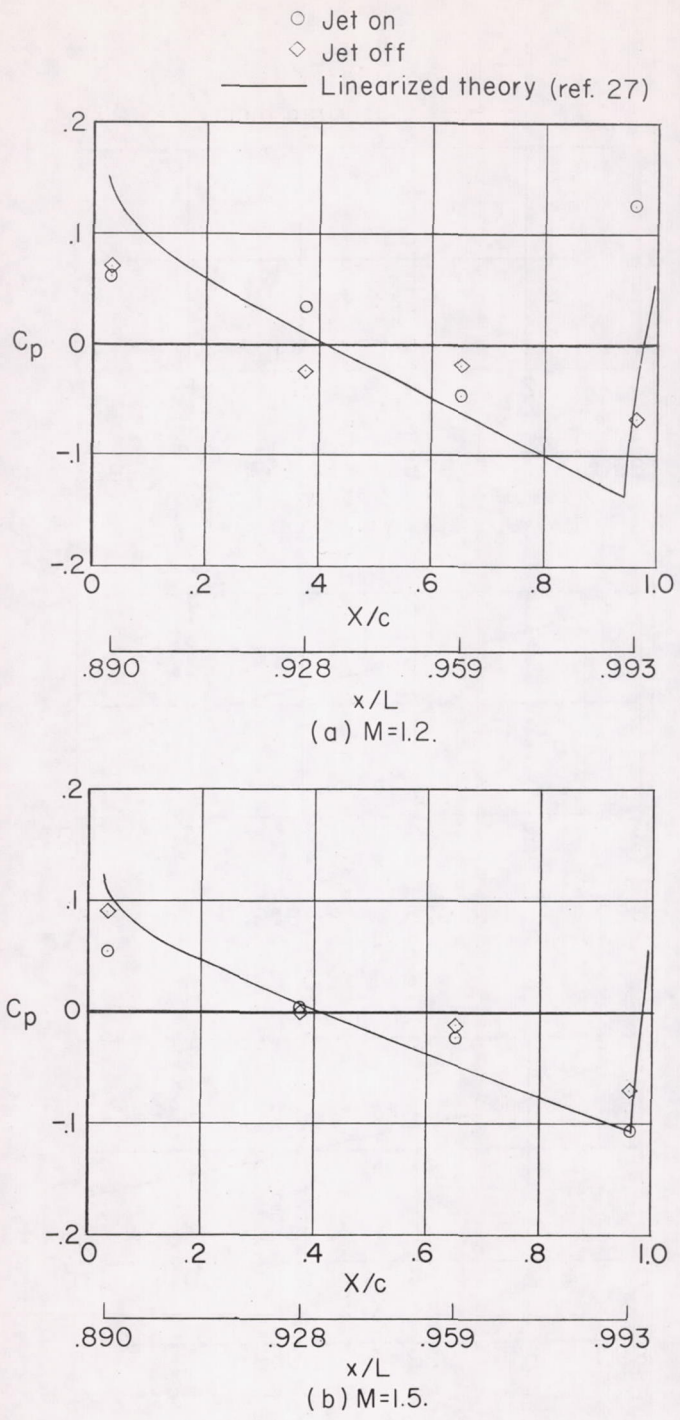


Figure 12.- Comparisons of the measured fin pressure coefficients at $\left(\frac{y}{b/2}\right)_{av} = 0.27$ of model A with the theoretical pressure coefficients obtained from linearized wing theory (ref. 27) at several Mach numbers.

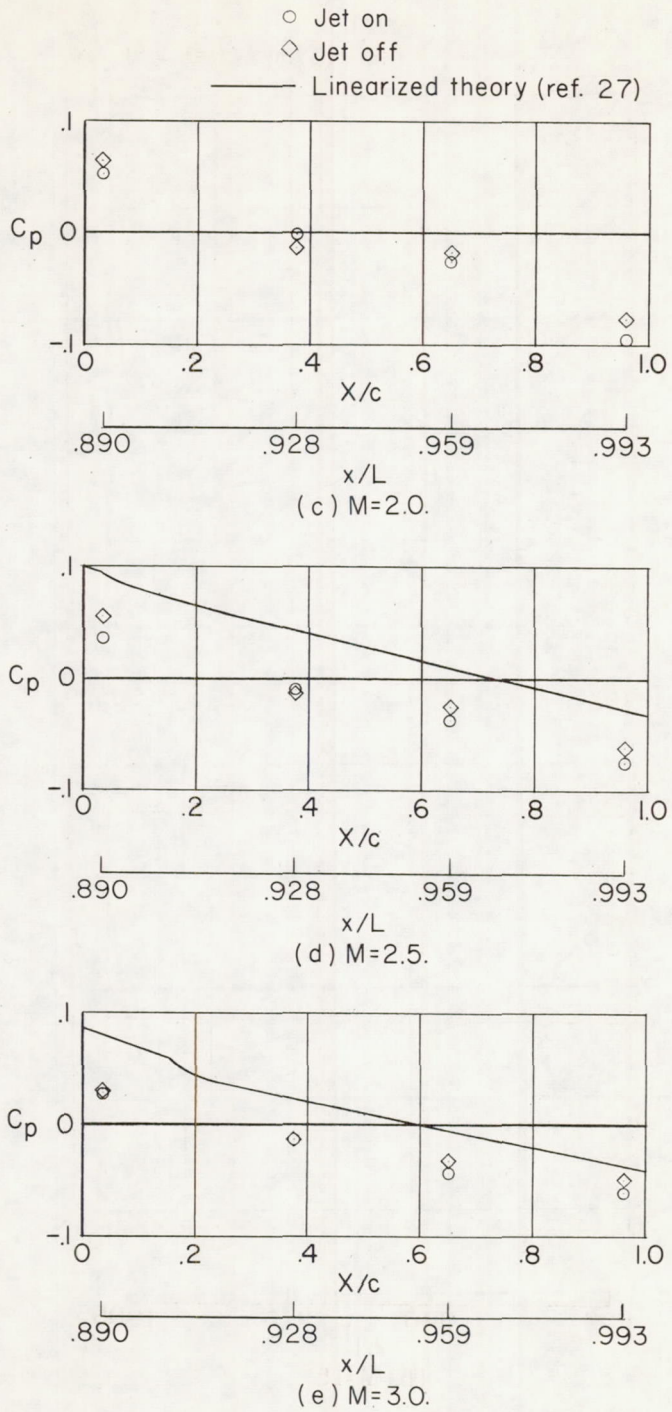


Figure 12.- Concluded.

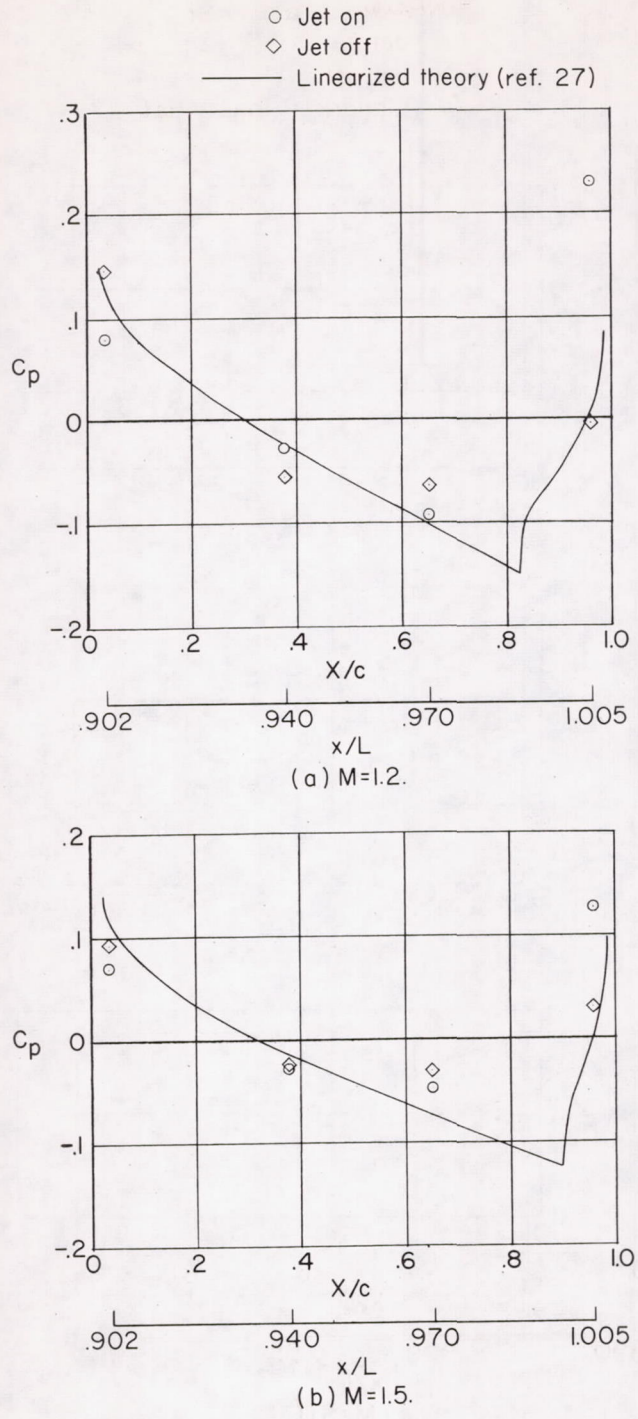


Figure 13.- Comparisons of the measured fin pressure coefficients at $\left(\frac{y}{b/2}\right)_{av} = 0.33$ of model A with the theoretical pressure coefficients obtained from linearized wing (ref. 27) at several Mach numbers.

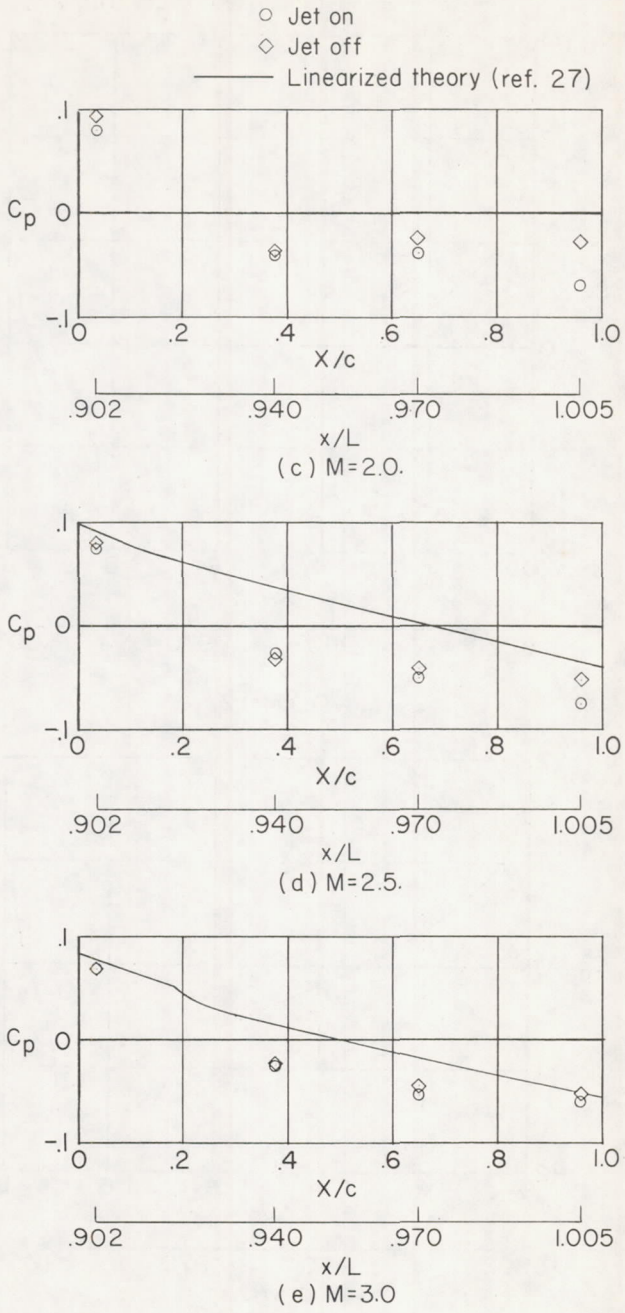
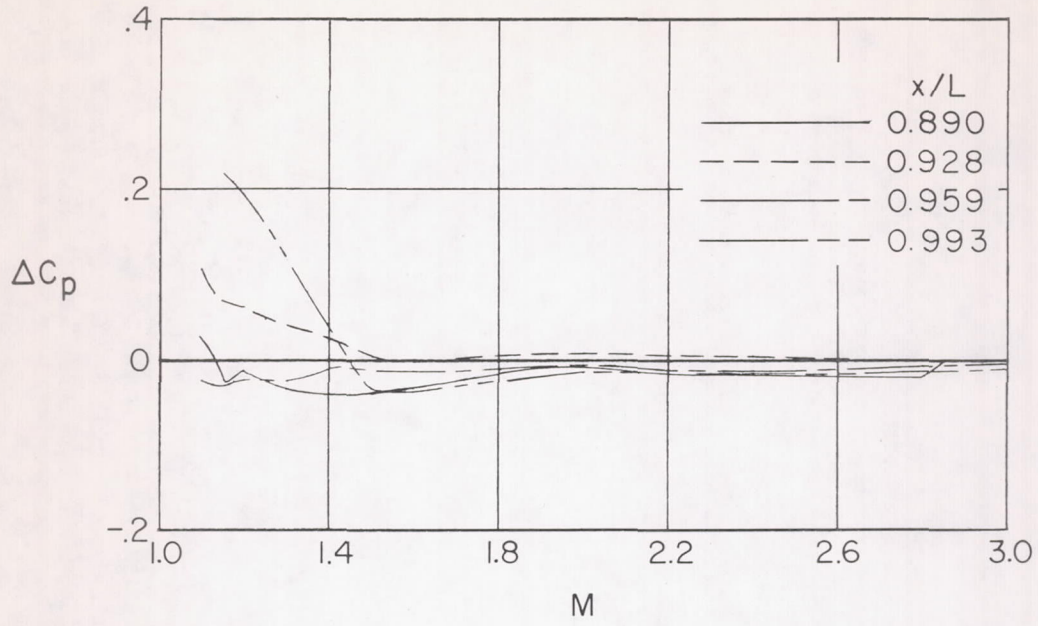
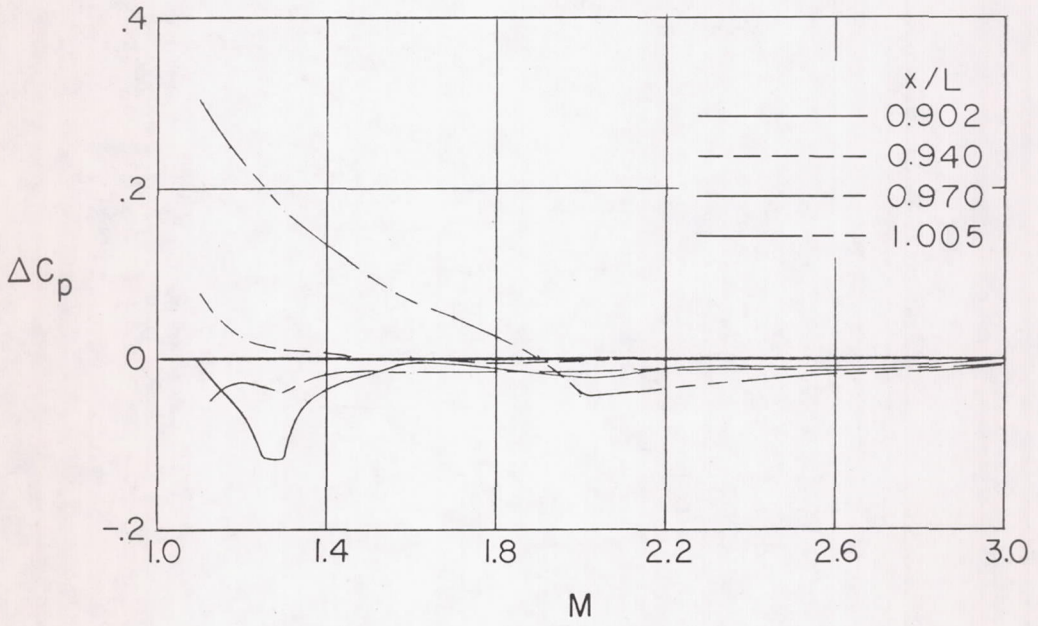


Figure 13.- Concluded.



(a) $\left(\frac{y}{b/2}\right)_{av.}$ =0.27.



(b) $\left(\frac{y}{b/2}\right)_{av}$ =0.33.

Figure 14.- Comparisons of the jet effects at the fin orifice stations of model A.

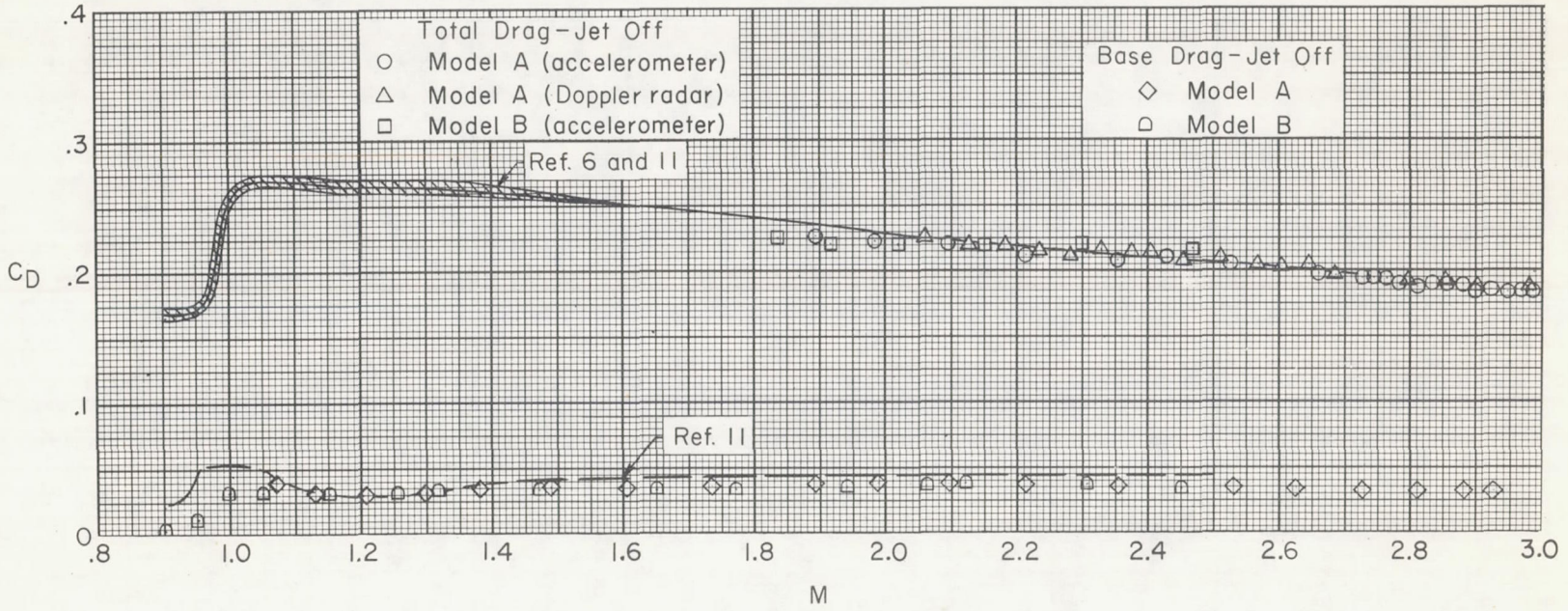


Figure 15.- Comparison of the variations of total-drag coefficient and base-drag coefficient with Mach number of models A and B for the jet-off flight condition.

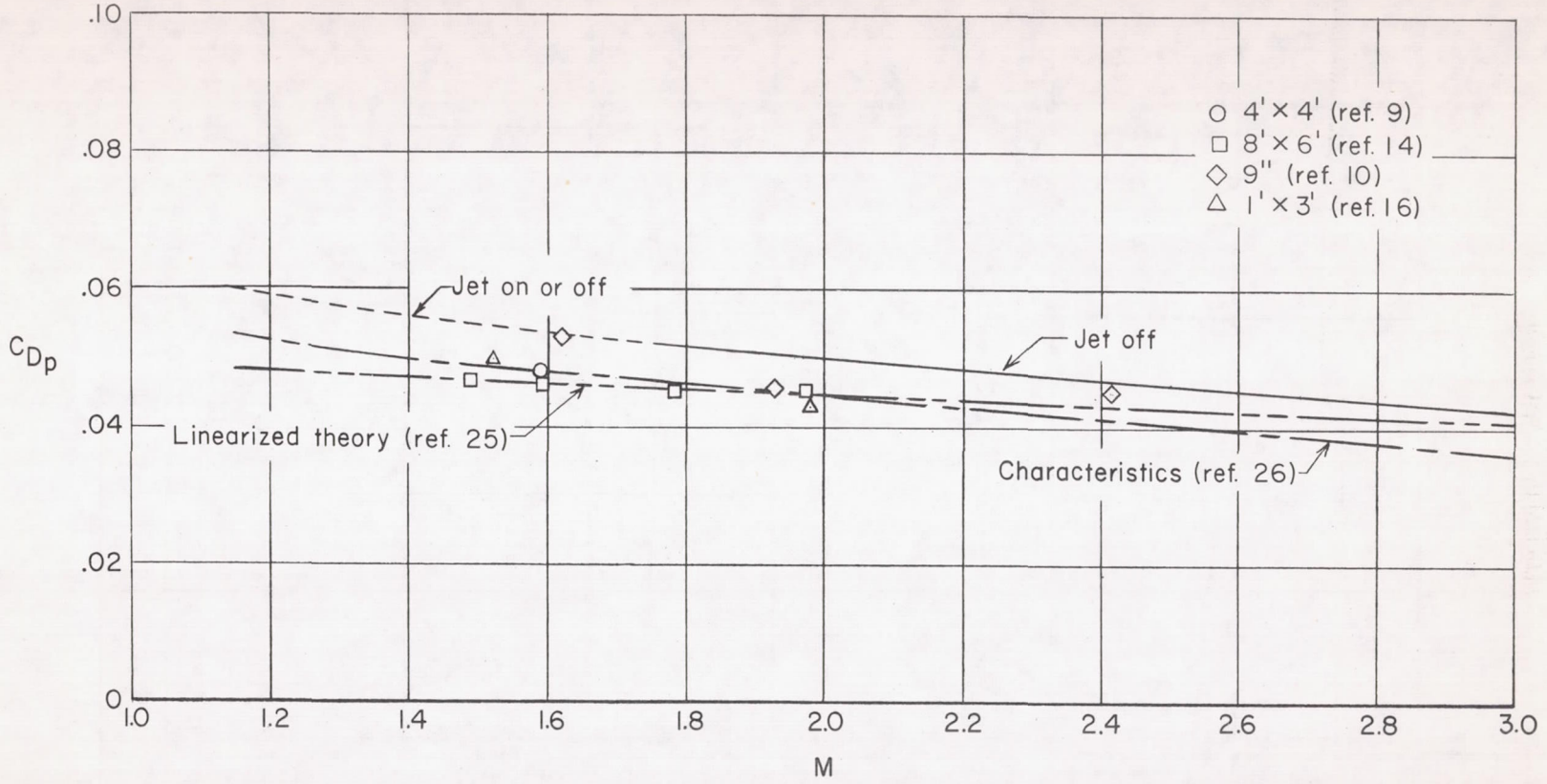
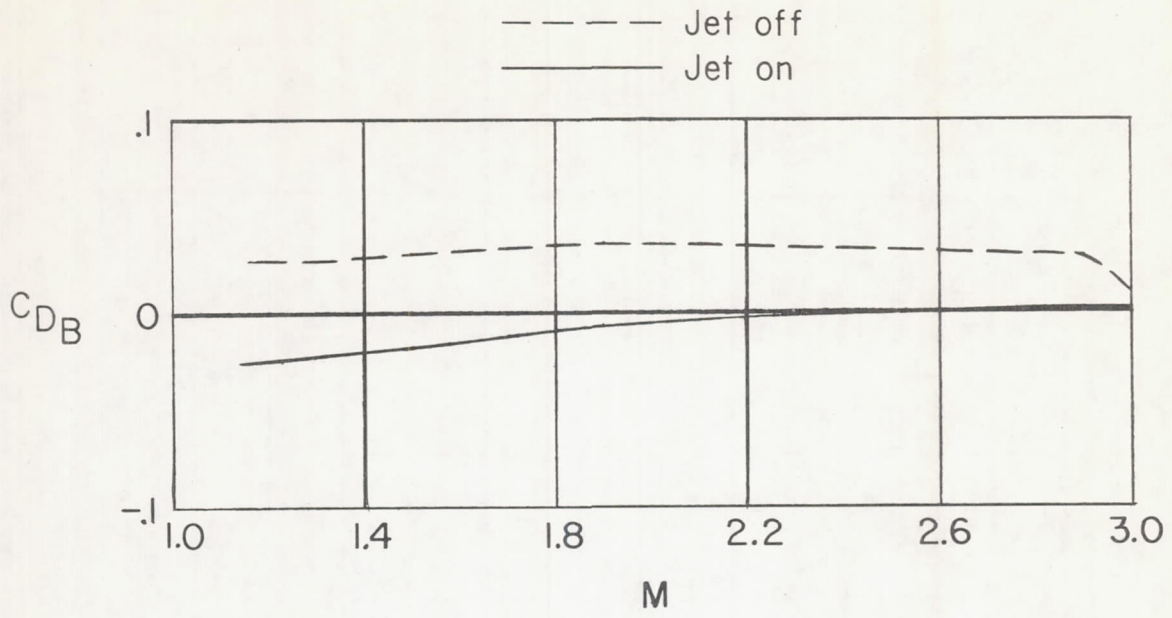
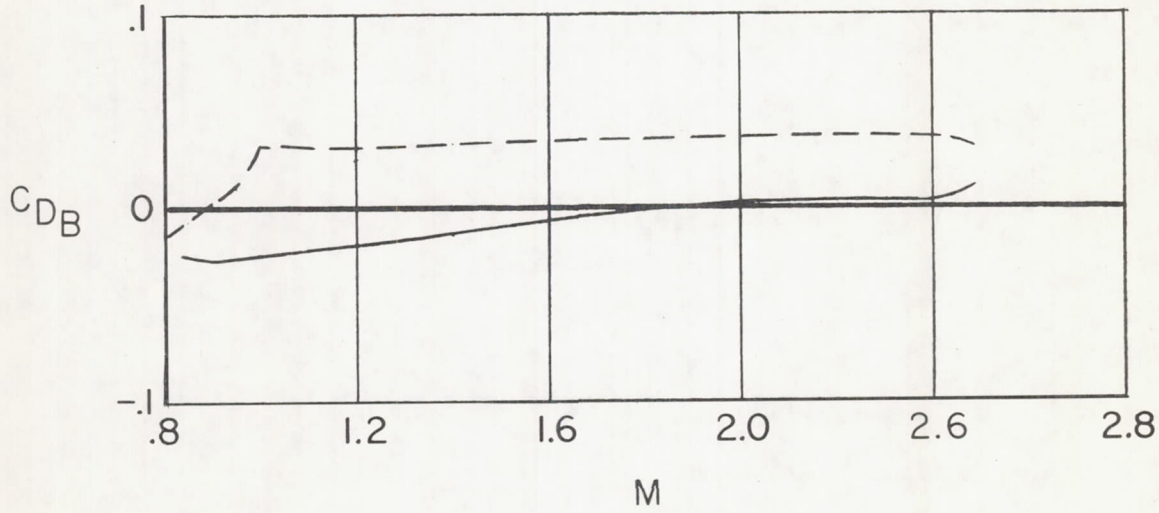


Figure 16.- Comparisons of the variations of pressure-drag coefficient with Mach numbers for the jet-on and jet-off flight conditions of model A with the pressure-drag coefficients from theory and wind-tunnel tests.

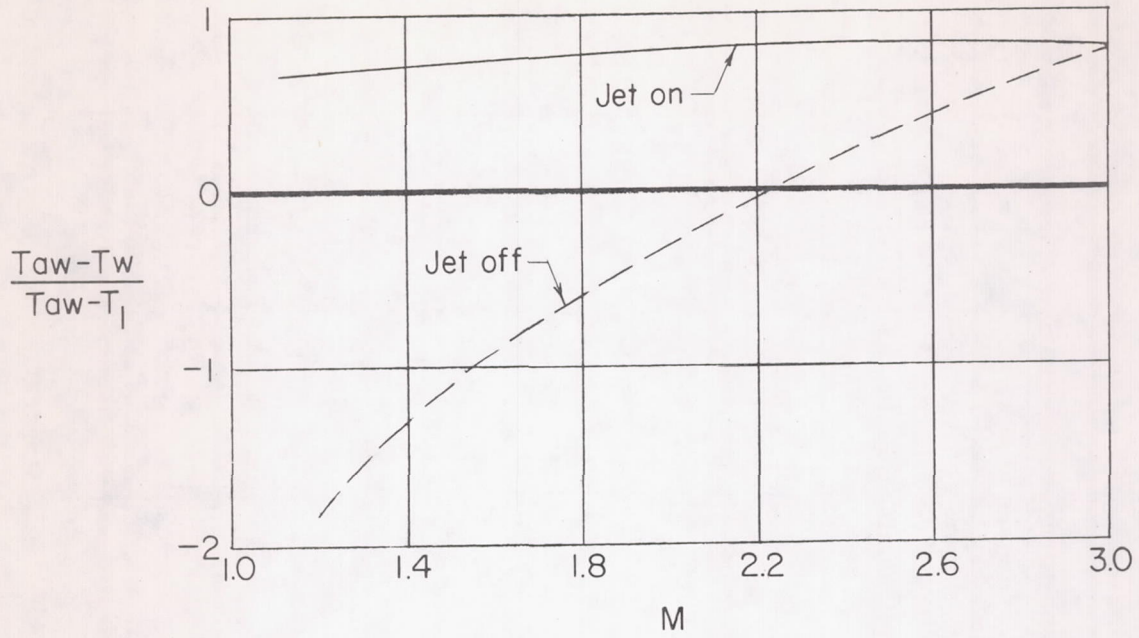


(a) Model A.

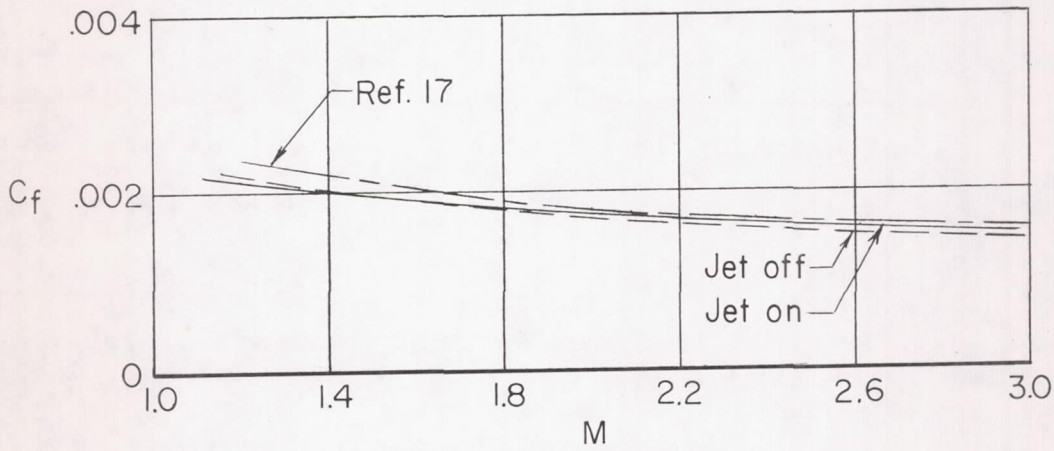


(b) Model B.

Figure 17.- Comparisons of the base-drag coefficients with Mach number for the jet-on and jet-off flight conditions of models A and B.

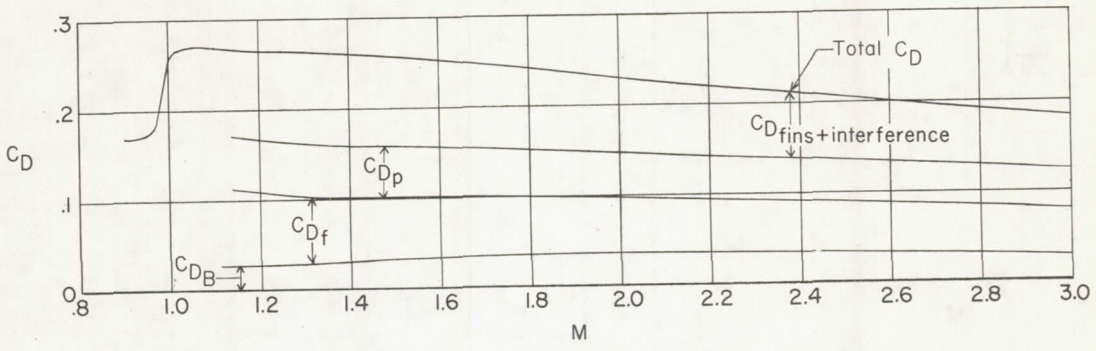


(a) Wall heating parameter.

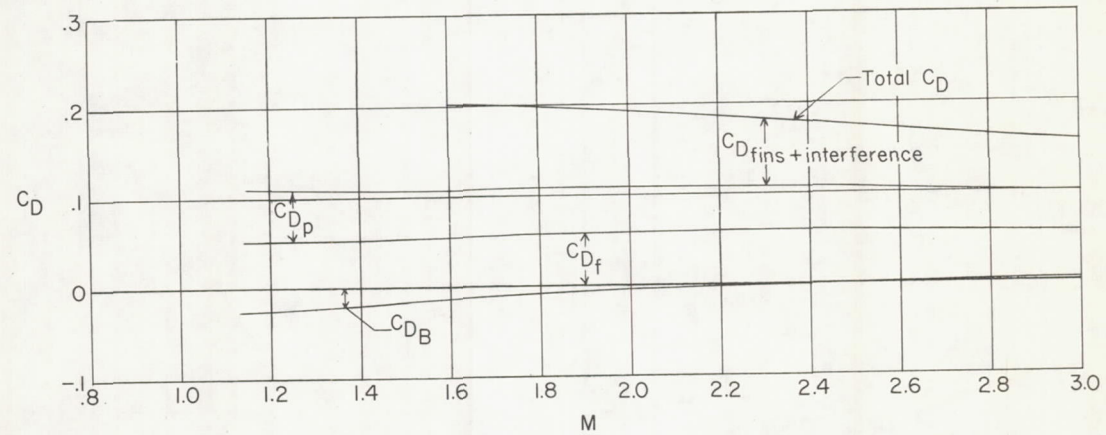


(b) Skin-friction coefficient.

Figure 18.- Variations of the computed wall heating parameter and skin-friction coefficient with Mach number (as determined from ref. 17) for the flight conditions of model A.



(a) Jet off.



(b) Jet on.

Figure 19.- A comparison of the total-drag coefficients for the jet-off and jet-on flight conditions of model A showing the magnitude of the base, skin friction, pressure, and fin-plus-interference drag coefficients through the Mach number range.

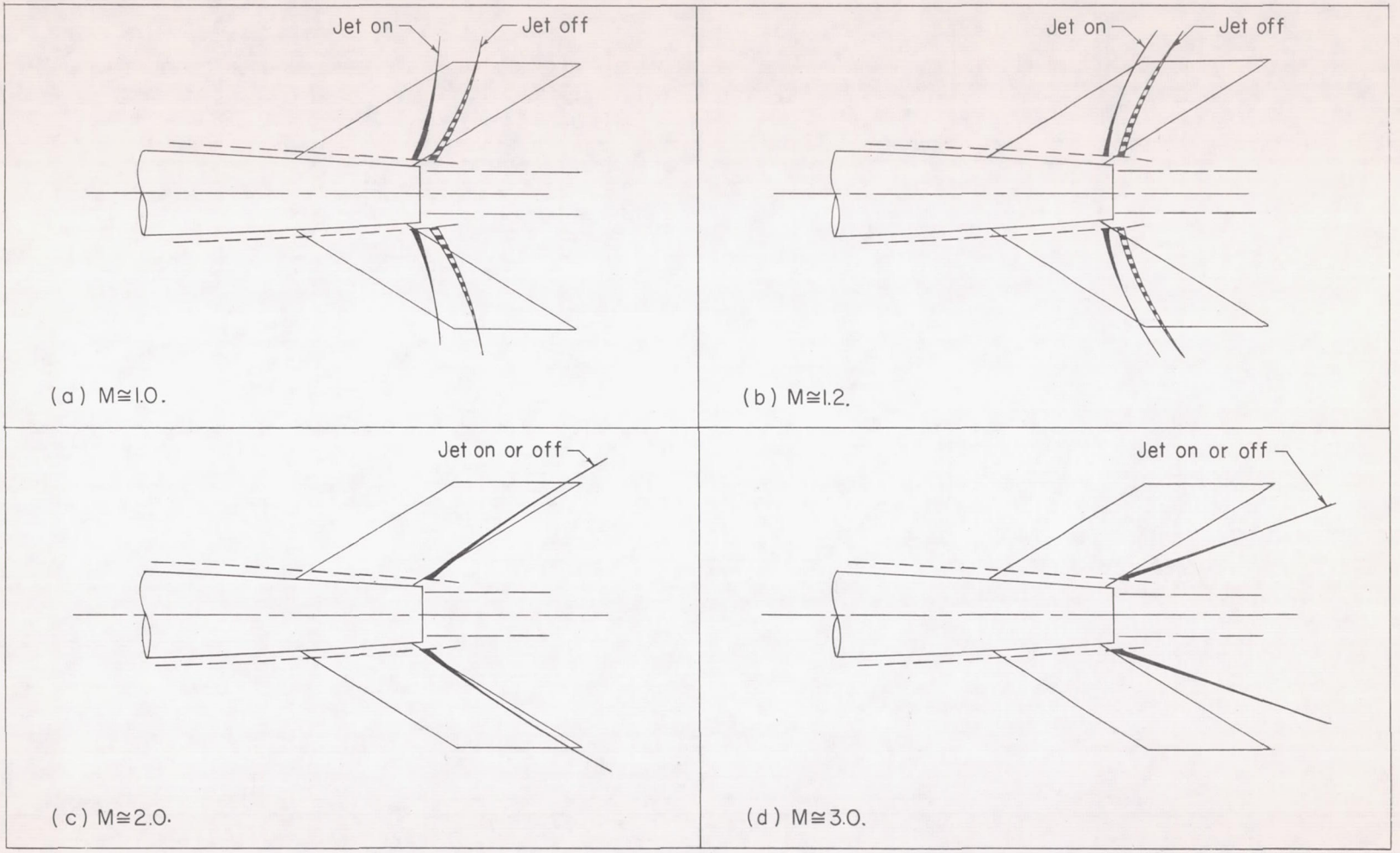


Figure 20.- Pictorial representation of the estimated location of the shock wave at the base of model A for the jet-off and jet-on flight conditions at several Mach numbers.